Experimental correlation of natural convection losses from a scale-model solar cavity receiver with non-isothermal surface temperature distribution

Ehsan Abbasi-Shavazi[1], Juan F. Torres[1], Graham Hughes[2], John Pye[1]

[1] Research School of Electrical, Energy and Materials Engineering, The Australian National University, ACT 2601, Australia

[2] Department of Civil and Environmental Engineering, Imperial College London, South Kensington, London SW7 2AZ, UK

ABSTRACT

Correlations for natural convection heat loss from solar cavity receivers are widely based on isothermal surface temperature assumptions, which do not occur in practice due to the local heat balance varying with position. An open question thus exists regarding the suitability of such correlations for non-isothermal conditions. This paper addresses this issue by presenting a new Nusselt correlation developed from an experimental investigation of natural convection heat loss from a non-isothermal model cylindrical cavity receiver. Cavities that are considered in this work have length-to-diameter ratios of 1 and 2, are operated at peak temperatures ranging from 355°C to 650°C, and exhibit temperature differences along the cavity wall between 40°C and 342°C. Stagnation and convection zones, as well as view factor profiles, are observed to contribute to the wall temperature distribution as the cavity is inclined downwards. An energy balance undertaken for steady state provides insight into the effects of non-uniform surface temperature distribution and inclination-dependent surface areas on radiative and convective losses. Natural convection heat loss results from this work are compared with widely-used correlations from the literature that assume isothermal wall conditions, and systematic discrepancies are observed. The proposed Nusselt correlation which accounts for the temperature non-uniformity, cavity inclination and geometric aspect ratio is evaluated against experimental data from this and other studies. It is found to produce excellent predictions of Nusselt numbers for cylindrical cavity receivers in the Grashof number range of 2.6×10^5 to 1.4×10^7.

Keywords

Natural convection heat transfer, Non-isothermal cavity, Cylindrical cavity receiver, Nusselt number correlation, Experimental heat transfer, Concentrating solar power (CSP).

1. Introduction

The energy transitions taking place across the world show a trend towards decarbonisation as renewable energy sources become the least-cost source of new generation (IEA, 2018). Factors such as dispatchability and low cost of thermal energy storage have enabled concentrating solar thermal (CST) technologies to be viewed favourably, culminating in research and development in this discipline across a number of decades (Apley, 1978; Braun and Edelstein, 1980; Falcone, 1986; Kolb, 2011). CST technologies capture and concentrate solar irradiation as a means of achieving the high temperatures required to operate electric power generation cycles (Behar et al., 2013; Zhang et al., 2013) or enable energy-intensive thermochemical reactions to occur (Steinfeld et al., 2017). Thermal energy storage is a key attribute of these systems, allowing for operation of large-scale power plants during intermittent periods of solar irradiation, thereby leading to increased capacity factors, improved grid integration and economic competitiveness for CST technologies. Efforts to reduce the levelised cost of electricity (LCOE) from CST power plants have seen renewed interest in recent years (ASTRI, 2017; Mehos et al., 2016).

The thermal efficiency of a solar receiver plays a significant role in the overall efficiency of photon-to-phonon energy conversion and hence can impact the LCOE of a CST power plant. The high temperatures at which a receiver operates often lead to increased thermal losses and, if adequate measures are not taken, can result in decreased receiver efficiency. Solar cavity receivers find frequent use in paraboloidal dish and central tower systems and can be subjected to large concentrations of solar flux. Efforts to increase the operating efficiency of this CST system component have included research on optimised receiver geometries (Asselineau, 2018; Pye et al., 2016; Shuai et al., 2008), utilising the natural variation of receiver surface temperature to reduce convection and radiation losses (Hughes et al., 2016), use of air curtains (Fang et al., 2019; Zhang et al., 2015), use of protective cowling as part of receiver structure (Cagnoli et al., 2019), use of partial or full windows on receiver aperture (Flesch, Robert et al., 2015; Maag et al., 2011; Uhlig et al., 2014), a variable aperture opening mechanism (Najafabadi et al., 2019; Van den Langenbergh et al., 2015), finned internal surfaces (Ngo et al., 2015) and cavity rotation (Wu, W. et al., 2014). Novel designs for externally-irradiated receivers used in central tower systems have also been proposed which use the cavity effect to reduce thermal losses (Ortega et al., 2017; Pye et al., 2018). In any attempt to lower LCOE by design improvement to receivers, the compromise between improved receiver design and necessary expenditure to implement the design complexities must be kept in mind so that end-goals relating to costs are not undermined.

Instrumental in any effort to increase the receiver thermal efficiency is the ability to accurately understand and model various thermal losses from a receiver. Convective losses from receivers are widely acknowledged to be more difficult to quantify than radiative and conductive losses. This is due to factors such as complex receiver geometries, large length scales with complex flow regimes and variable ambient conditions, among many others, that can influence the convection heat transfer coefficient. Following the early activities regarding design and use of CSP systems, a detailed report summarising findings of the research initiatives focusing on developing sought-after predictive tools for quantifying convection loss from solar thermal receivers was collated by Falcone (1981). Clausing (1981, 1983) and Clausing et al. (1987) undertook ground-breaking analytical and experimental investigations of thermal loss from cavities and noted that

the transfer of mass and energy across the aperture, as well as the ability to heat the air inside a cavity, influenced convection heat loss from solar receivers. In the two latter studies, a cryogenic test facility was used to conduct experiments with Rayleigh numbers as large as 2×10^{11}, which are representative of convection regimes encountered in operational solar thermal receivers. The cryogenic experiment environment assisted in controlling the ambient temperature T_∞ to values between 80 K and 310 K, thereby masking radiative heat transfer effects (Clausing, 1982). Experimental data from these studies led to the development of complex analytical relations for convection heat loss from cavity receivers. An implicit function b was defined in their work which accounted for values of bulk cavity air temperature T_b which are significantly different than T_∞ (see Nomenclature section for the complete formulation of this function b). While the use of cryogenic testing environments allow for the specific consideration of convection heat transfer (Clausing, 1982; Flesch, R. et al., 2015), numerous studies have commented on the conjugate relation between the heat loss mechanisms of radiation and convection in open cavities, e.g. (Montiel-Gonzalez et al., 2015; Polat and Bilgen, 2003; Xamán et al., 2009). Therefore, it is important that studies of convection heat transfer also be undertaken at the elevated temperature conditions encountered in CSP receivers, so as to provide an understanding of high-temperature effects on this loss mechanism (Wu, S.-Y. et al., 2014).

Following on from the work of Clausing, researchers have proposed various Nusselt number correlations for the estimation of convection losses from receivers based on isothermal wall assumptions, which is actually a rare condition in solar thermal applications. Given the empirical nature of these correlations, one distinguishing feature is their formulation is much simpler than the analytical relation proposed by Clausing. Harris and Lenz (1985) reported a correlation based on experimental data from on-sun tests undertaken by Koenig and Marvin, which considered the effect of inclination angle and Rayleigh number on convection losses. Research by Stine and McDonald (1989) on a receiver with cylindrical and frustum sections led to the proposal of a correlation that was an extension of the model proposed by Siebers and Kraabel (1984), which accounted for variable thermophysical properties, but which additionally included a ratio of geometric lengths to model different receiver internal surface and aperture areas as well as a factor to account for cavity inclination. Ensuing work by Leibfried and Ortjohann (1995) using experimental data from downward and upward-facing spherical and hemispherical cavities led to modifications to the correlations proposed by Clausing et al. (1987) and Stine and McDonald (1989). The parameters which were introduced allowed the correlations to better capture the effect of reduced aperture size and cavity geometry on air circulation within a heated cavity.

Numerous studies have commented on the ability of the Clausing correlation to provide consistently better estimates of convection losses due to the formulation of convective and stagnant zones, the areas of which are dependent on the cavity inclination. Fig. 1 schematically shows these two zones. Clausing (1981) hypothesised that in an inclined cavity, a stagnant volume of heated air forms above a horizontal free-shear layer which intersects with the highest point of the upper lip of the cavity aperture. In calculating the resulting convective heat loss from the cavity, Clausing noted that the surfaces positioned below the horizontal free-shear layer contribute significantly to this heat loss mechanism.

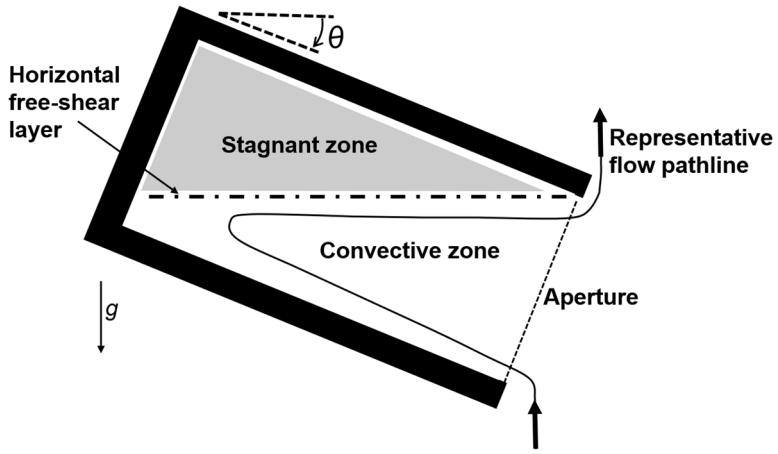

Fig. 1. Schematic representation of stagnant and convective zones within an inclined heated open-aperture cavity.

An important contribution to this area of research was produced by Prakash et al. (2010) who first undertook experimental work on developing a parameter termed the *critical air temperature gradient* to quantify the extent of stagnation and convective zones. This parameter was based on experimental data obtained from air temperatures within the cavity volume and supported the hypothesis proposed by Clausing. The utility of this parameter lies in informing the design process relating to layout of active heat transfer surfaces within a cavity receiver. Paitoonsurikarn et al. (2011) suggested an alternative characteristic length definition, termed the *ensemble length,* which sought to circumvent the calculation of the inclination-based surface areas for the calculation of convection heat loss. The resulting correlation was refined using a numerical parametric study of three cavity receivers. However, as the ensemble length was defined based on a limited set of geometries, its respective correlation has been reported to under- or over-estimate the convection loss in a number of cases (Samanes et al., 2015; Uhlig et al., 2014; Wu, W. et al., 2014). Jilte et al. (2013) undertook a numerical investigation of seven different cavity geometries assuming isothermal boundary conditions and, after investigating the correlation between convection loss and different surface area definitions, proposed a correlation based on an inclination-dependent surface area specifically defined as the summation of the lateral and back wall surface areas below the horizontal free-shear plane and the area bounded by the cavity walls and the horizontal free-shear plane. In a subsequent experimental work, Jilte et al. (2017) used a differentially-heated cylindrical cavity receiver which was specifically built to ensure that isothermal wall conditions were met. However, the authors did not provide results showing the accuracy with which their previously reported correlation could predict their experimental results, and instead proposed a new Nusselt number correlation that could be used in conjunction with the aperture area—a constant parameter with regard to cavity inclination angle—to calculate convection heat loss. A useful review of natural convection correlations for solar cavity receivers of different geometry is collated by Wu et al. (2010).

In addition to using thermal loss analysis to determine influential factors contributing to convection, visualization studies have also been undertaken to obtain physical insight into the role of parameters such as cavity geometry and inclination on convective flows and losses from open cavities. Leibfried and Ortjohann (1995) used smoke and light ash particles entrained in the streaming air to visualise circulating flow patterns and convective zone dynamics within two open

cavities of different geometries. These insights were used in developing characteristic length definitions as well as cavity surface area ratios for use in correlations reported as part of their research. Taumoefolau et al. (2004) used the Synthetic Schlieren technique (Dalziel et al., 2000) to visualise the convective flows at the aperture and compared the results with numerical simulations. Comparison of instantaneous and time-averaged Schlieren images showed that the plume was steady as it left the cavity and became unsteady above the model receiver. The numerical simulations showed that the fraction of the aperture area taken up by convective flow exiting the cavity decreased as the cavity axis was inclined downwards. Yeh et al. (2005) studied a rectangular cavity with transparent Perspex sides in a water tank and used salinity variations to model temperature gradients. This can be considered to be a unique approach to circumventing the complexity of experimentally modelling the density ratios between air entering a cavity and air at the temperature of the heated surfaces, which can typically be a factor of three to four (Clausing, 1981). The experimental setup allowed flux-based Grashof values between 7×10^4 to 10^{10} to be studied. Injection of dye close to the aperture allowed the authors to visualise fluid flow into and out of the cavity, and also observe the formation of convection and stagnation zones within the cavity at different inclinations.

Ambient conditions and, more specifically, the lack of steady flows in the atmospheric boundary layer, complicate convective heat loss analysis of receivers that operate in on-sun conditions. The geometric length scales encountered in CSP receivers renders both natural and forced convection effects important in design and performance analysis of these systems (Torres et al., 2018; Torres et al., 2020). Researchers have used laboratory-scale experiments or numerical models to examine how losses and receiver performance are affected by mixed convection (Cagnoli et al., 2019; Flesch, R. et al., 2015; Lee et al., 2018; Lee et al., 2017; Ma, 1993; Prakash et al., 2009; Siebers and Kraabel, 1984; Torres et al., 2018; Xiao et al., 2012). The observed trends vary depending on parameters such as receiver inclination, geometry and wind conditions (speed, direction, turbulence intensity). Nevertheless, a major finding from these studies is that in certain scenarios, mixed convection heat loss from receivers can decrease below the value of natural convection as a result of boundary layer thickening and flow separation. The exposure of inclined heated surfaces to air flows of different velocity and direction—as encountered in natural, mixed or forced convection regimes— in addition to higher radiative loss near the aperture contributes to the observed non-isothermal temperature distributions, which must be studied in more detail to obtain a clearer understanding of the dynamics of receiver convection heat loss.

A review of the literature summarised above revealed that detailed investigations on convection loss from non-isothermal cavity receivers are scarce. Most experimental studies have focused on isothermal conditions, or merely given mention to average cavity temperatures without providing a detailed description regarding the temperature distribution encountered in the receivers. Boehm (1987) presented a summary of convective heat loss results from operational solar central receivers, and noted that flux-on and flux-off techniques that are used to quantify thermal losses result in different surface temperature distributions and thus lead to discrepancies in convection estimates. Ries et al. (1995) undertook an analytical investigation of non-isothermal receivers and showed improved efficiencies for certain non-isothermal receivers. Following this work, Kribus et al. (1999) presented experimental results from a multistage, non-isothermal receiver. In a study focusing on the design of a solar gas reformer, Liovic et al. (2014) used CFD

models in addition to convection correlations to obtain an estimate of losses from this cavity-shaped reactor. They stated that the inability of empirical correlations to properly account for non-uniform temperature distributions, as well as their geometry-specific basis, resulted in significantly different predictions between the correlations. Yuan et al. (2015) highlighted that the simplistic assumption of isothermal or constant flux boundary conditions in simulations of large-scale solar cavities could result in experimentally-derived convective losses being underestimated by up to 50%. On this basis, use of non-uniform temperature distributions in energy balance models could improve thermal loss estimates from solar cavities. A number of experimental and numerical investigations have been undertaken that use the boundary condition of constant heat flux applied to various combinations of the side and back wall surfaces in cylindrical cavities (Shen et al., 2015; Wu et al., 2013; Wu, S.-Y. et al., 2014; Wu et al., 2015a; Wu et al., 2015b; Xiao et al., 2020; Xiao et al., 2012) and semi-cylindrical cavities (Chakroun, 2004; Chakroun et al., 1997; Chakroun and Quadri, 2002). Results showing non-isothermal temperature profiles along the cavity side wall form one of the important findings from these studies. Hughes et al. (2016) implemented a non-isothermal temperature profile as boundary condition for a numerical study of a cavity receiver and noted that the ensuing heat flux results showed that utilising the naturally-occurring variation of temperature across a cavity surface could present opportunities for the recuperation of losses within a cavity, thereby improving the receiver thermal performance. Lin et al. (2018) presented results from a numerical study in which, among other parameters, the presence of a cooled receiver front was investigated in an effort to increase receiver efficiency. While results from their work showed slightly reduced efficiencies when the cooled receiver front was employed in the model, they maintained that for receivers at scale, this influence could be rendered insignificant, given the practical outcome of limiting damage caused by spillage irradiation at the receiver front. Najafabadi et al. (2019) present an experimental study in which, while acknowledging the presence of temperature non-uniformity in a solar cavity reactor, propose design modifications to reduce this effect to enable higher performance efficiencies. Recently, Lee et al. (2019) has studied the concept of temperature non-uniformity in a receiver, and shown an increase of up to 70% in convection losses for some non-isothermal temperature distributions in comparison to isothermal cases. However, the data reported in their work relates to one specific cavity inclination and a convection heat loss correlation which can be used for predictive purposes is not provided. In summary, while numerous studied have highlighted the presence of non-uniform temperatures across cavity surfaces, the temperature distributions used in most of the literature relating to cavity convection heat loss models are not representative of conditions encountered in CST applications, and thereby lead to inaccurate estimates of this thermal loss mechanism in the process of receiver design and performance modelling. This forms the motivation for a more detailed study on the topic.

The objectives of this paper are, firstly, to provide experimental data relating to cases of non-isothermal temperature distribution in heated cylindrical cavities and to discuss the mechanisms by which these non-isothermal temperature profiles arise; secondly, to compare the experimental data with natural convection correlations which assume isothermal cavity walls and comment on any discrepancies that are observed; and thirdly, to propose a revised Nusselt number correlation for natural convection heat loss that is based on the insight obtained from experiments conducted as part of this work. In meeting these objectives, the layout of the paper is as follows: Section 2 presents the experimental setup and introduces the methodology that is used to acquire

and process the experimental data. Section 3 presents the analysis on the measured temperature distribution in the heated cavity, as well as a discussion of observed trends in thermal losses across different inclination angles and cavity temperatures. Additionally, convection losses are compared with estimates obtained from Nusselt correlations reported in the literature and trends are discussed. Lastly, Section 4 presents a revised Nusselt number correlation that considers cavity temperature non-uniformity and is based on experimental data obtained from the current study as well as data extracted from other experimental cylindrical cavity studies reported in the literature. The ability of the proposed correlation to provide accurate estimates of convection heat loss from large-scale cavity receivers is highlighted using experimental data from three different case studies reported in the literature.

2. Experimental setup and methods

2.1. *Experimental setup*

The motivation for undertaking the experimental campaign in this work was to establish temperature distributions within a cavity and analyse trends in the resulting thermal losses, at different operating conditions. The experimental setup that was designed for this purpose and used to acquire data for this study is shown in Fig. 2. In addition, a schematic diagram that shows the different components of the model cylindrical cavity receiver is shown in Fig. 3. Some design aspects of this setup were reported in previous publications (Abbasi-Shavazi et al., 2015; Hughes et al., 2016). The model receiver consists of a stainless steel-316L cylindrical cavity, with internal diameter D of 83 mm and wall thickness of 3 mm. Two such cavities were used during the

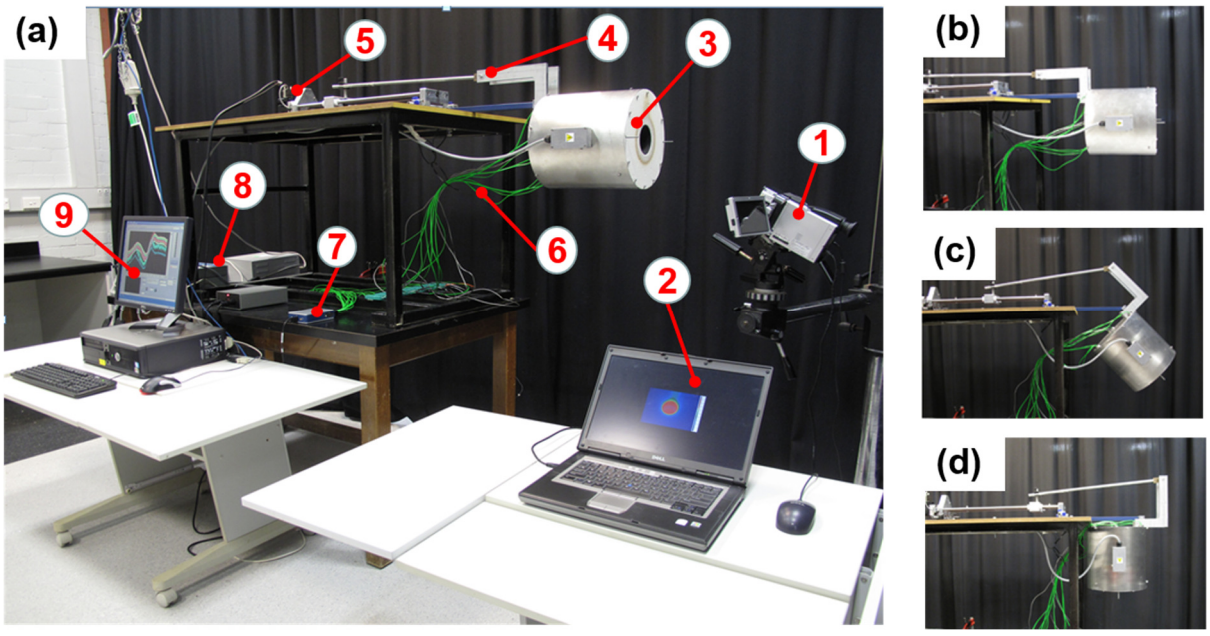

Fig. 2. Experimental setup for natural convection experiments. **(a)** 1: Thermal imaging camera, 2: Laptop used for thermal image acquisition, 3: Model cavity receiver, 4: Mechanism for varying the inclination of the model receiver, 5: Stepper motor, 6: Thermocouple connections, 7: Data logger, 8: Power controller, 9: Computer used to record data. **(b)-(d)** Cavity inclined at $\theta = 0°, 45°, 90°$.

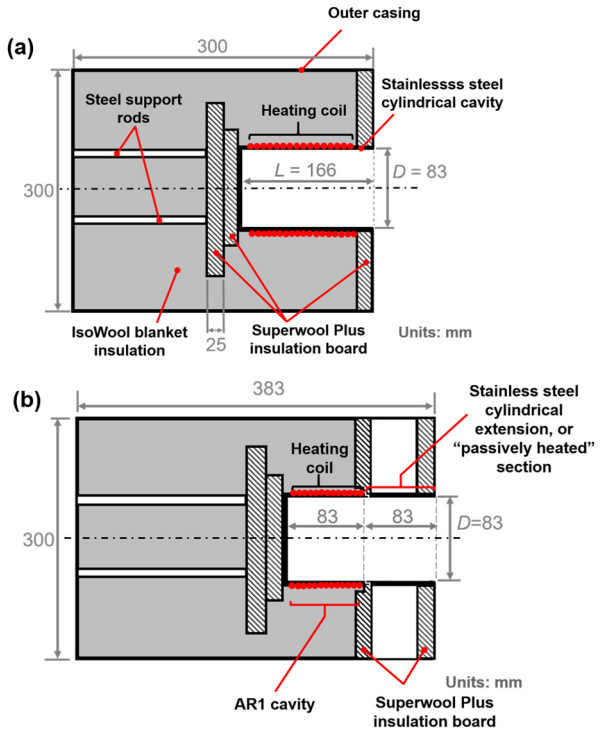

Fig. 3. Cross-section of cylindrical cavity assemblies, showing different components of **(a)** AR2 and **(b)** AR2* cavity. Note that the AR1 cavity is the section exposed to the heating coil and embedded in the blanket insulation, as part of the AR2* cavity assembly. Note that in part (b), the AR1 cavity was built and used in experiments, prior to the attachment of the passively heated section which resulted in the formation of the AR2* cavity.

experimental campaign, with lengths L of 83 mm and 166 mm, resulting in aspect ratios AR (L/D) of 1 and 2, respectively. The cavities used in the experiments were heated by Pyrotenax® magnesium oxide-insulated, stainless steel-sheathed heating cables having a nichrome conductor (Model HSQ1M4000). Good thermal contact between the cavity outer surface and the heating cable was obtained by tightly winding the cables around the cavity and fastening them to the outer cavity surface. In order to increase the degree of temperature inhomogeneity in the cavity, additional experiments were conducted using an 83-mm long cylindrical extension of the same material, diameter and wall thickness as the original cavity, which was attached to the aperture of the AR1 cavity. This configuration is schematically shown in Fig. 3(b), and is henceforth referred to as the AR2* cavity. The extended section is neither subjected to direct heat input via contact with the heating cable, nor is it covered by blanket insulation. This ensures a larger reduction of temperature in the front section of this cavity in comparison to the AR2 cavity, which is heated along its full length by a heating coil. The method employed in this work to obtain a temperature distribution in the cavity can be considered as an alternative approach to differential heating of the cavity, as used in other studies (Jilte et al., 2017; Lee et al., 2019).

Pyromark-2500 flat-black solar-grade heat resistant paint (Ho et al., 2012) was used to coat the inner surface of the cavities, yielding known surface emissivity properties ($\varepsilon = 0.87$) that were used in the radiation heat loss calculations. To ensure good adhesion of the paint to the cavity surface, sandblasting was performed using ABSS #4 glass beads (approx. 150–250 μm in diameter). Using a tactile/visual surface roughness comparator, the roughness of the uncoated pipe is seen to be between surface roughness grades of N6 and N7, which translate to arithmetic

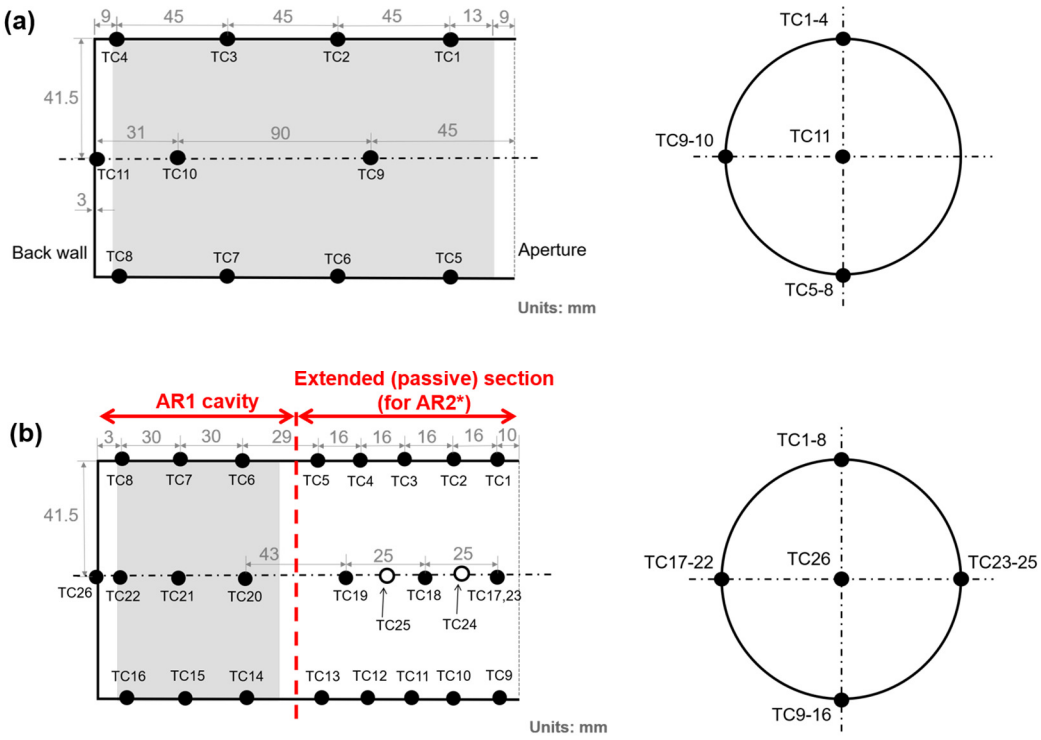

Fig. 4. Side-view (left) and front-view (right) schematics showing location of thermocouples (TC) for **(a)** AR2 and **(b)** AR2* and AR1 cavities. Shaded regions represent sections of each cavity which were heated using electrical heating coils.

mean surface roughness R_a values between 0.8–1.6 μm. The paint was applied using a brush to the surface of the cavity, which was dry and at room temperature. To obtain maximum thermal properties, heat curing was performed as specified by the paint manufacturer, which involved heating the surface at 250°C for two hours after the paint had air-dried for 18 hours. After the heat curing, vitrification was performed by raising the temperature from 250°C to 500°C over a 15-minute period. This process ensures protection of the surface against subsequent conditions of heat shock which might be induced by fast heating. Insulation was used to reduce conduction heat loss from the side and back of the cavity, as seen in Fig. 3. Two circular Superwool Plus insulation boards (k = 0.09 W/m·K at 400°C), each of 25 mm thickness but with different diameters, were attached to the unheated back wall of the cavity. The remaining volume between the cavity and outer casing was filled with layers of Isowool ceramic fiber blanket insulation (k = 0.07 W/m·K at 400°C). The primary intended application for our research is dish concentrators, but the findings also apply to tower systems with cavity receivers. For this reason, our apparatus, while easily reconfigurable, is designed for operation at downward-facing inclination angles in the range 0°–90°, which is the full operational range of the receivers in dish systems. In the case of fixed tower receivers, higher optical efficiencies are obtained when receivers are inclined towards the centre of the heliostat field (Wang et al., 2019). This angle is usually between 0°–35°. To allow tilting of the cavity to different downward inclinations, a rotating hinge attachment at the back of the receiver was connected to a stepper motor and a lead screw using two aluminium angles and a guiding rod, as shown in Fig. 2(a). The rotary displacement of the stepper motor was calibrated against the range of required inclination angles. A Eurotherm 3058 power controller delivered constant

electrical power to the heating cable. An Emtek EDW-6000 true power meter (±1% reading accuracy) was used to cross-check the electrical power supplied from the Eurotherm unit.

The wall temperatures in each cavity were measured using thermocouples located as indicated in Fig. 4 (note that the AR1 cavity is shown as part of Fig. 4b). The measuring junction of each K-type thermocouple (Class 2) was placed in a hole which was drilled into the cavity outer surface and terminated 1 mm from the inner surface. The thermocouples were then brazed into place. Ten and eleven thermocouples were used to measure the cavity wall temperatures in the AR1 and AR2 cavities, respectively. An additional two thermocouples were embedded in the surrounding insulation and were used to measure the side- and back wall temperature of the receiver casing for both cavities (not shown in Fig. 4). For the AR2* cavity, a total of 26 thermocouples were used to measure temperatures at different locations along the cavity wall. Temperature data was recorded with a sampling rate of 2 Hz using a National Instruments™ 9213 data logger. An NEC H2640 infrared thermal imaging camera was used to visually inspect the cavity wall temperature distribution. A LabVIEW™ program was used to operate the power controller, record temperature data from thermocouples and control the receiver inclination for each experiment.

2.2 Experimental procedure

The experiments were conducted with the Eurotherm power controller being used to set the electrical input power to the heating cable and thereafter allowing the heated cavity to reach steady-state condition. For the purposes of this study, a steady-state condition was deemed to be attained when the rate of temperature change was less than 1°C/h for all thermocouples embedded along the cavity wall and within the receiver casing. The inclination angle θ of the model receiver was varied from $\theta = 0°$ (horizontal cavity) to $\theta = +90°$ (vertically downward-facing cavity), in increments of 15°. In order to obtain different meaningful datasets during the experiments, two specific approaches for heating the cavity were used.

In the first approach, the total power values that were needed to deliver a peak local temperature in the cavity equal to 500°C, 570°C or 650°C at $\theta = 90°$ were determined. These temperatures were chosen to produce different datasets that could be used in developing a new correlation that spanned a range of Grashof numbers. In the subsequent experiments, the input power to the heating cable was kept constant at each of the determined power values and steady-state temperatures in the cavity were recorded for the range of inclination angles. Based on the relative size of convection and stagnation zones at each inclination angle, the temperature distribution changed and thus different peak and average cavity temperature values were recorded across all inclination angles. In this approach, the temperature of the cavity was not actively controlled as in (Lee et al., 2019). This approach was used for the AR1 and AR2 cavities.

In the second approach, the peak temperature of the cavity was kept constant at values of 495°C, 570°C, 597°C or 650°C for the full range of cavity inclinations by manually varying the input power to the heating cable. These temperature values were chosen to have different ratios of convection to radiation, and different wall temperature profiles to those obtained using the first approach. Furthermore, it allowed for the acquisition of datasets at different Grashof numbers. This experimental approach was used for the AR1 and the AR2* cavities.

The experiments were conducted in a controlled laboratory setting that was isolated from ambient air currents. A number of experiments were repeated on two occasions to assess repeatability of the data. It was found that the steady-state temperature at the location of each thermocouple on the cavity wall was within ±0.1°C over successive experiments, signifying the quality of the data and the acquisition process.

2.3. Determination of energy balance

As previously mentioned, a large temperature inhomogeneity was introduced on the cavity surface by attaching an uninsulated cylindrical extension to the AR1 cavity. The extension gained heat mainly via heat transfer from the heated AR1 cavity and lost heat to the ambient from its external uninsulated surface. Fig. 5 schematically shows the rationale for using this approach. Fig. 5(a) shows a representation of a cavity which is subjected to a uniform heat input along its full length which results in a representative temperature distribution $T(x)$. This resembles the condition in the AR1 and AR2 cavities. As shown in Fig. 5(b), when separate sections of the cavity are subjected to different heat inputs, such as a positive heat input and a negative heat input (*i.e.* heat removal), the temperature distribution can change markedly. This condition is encountered in the AR2* cavity, whereby the heating coil provides the positive heat input, while radiation and convection heat loss from the external surface of the extension constitute heat removal from the cavity. In this work, the aim is to establish different temperature distributions in cavities and thereafter determine the radiative emission and convection losses through the cavity aperture arising from each temperature distribution. As such, the method by which a temperature distribution arises is immaterial, as long as the losses can be determined accurately.

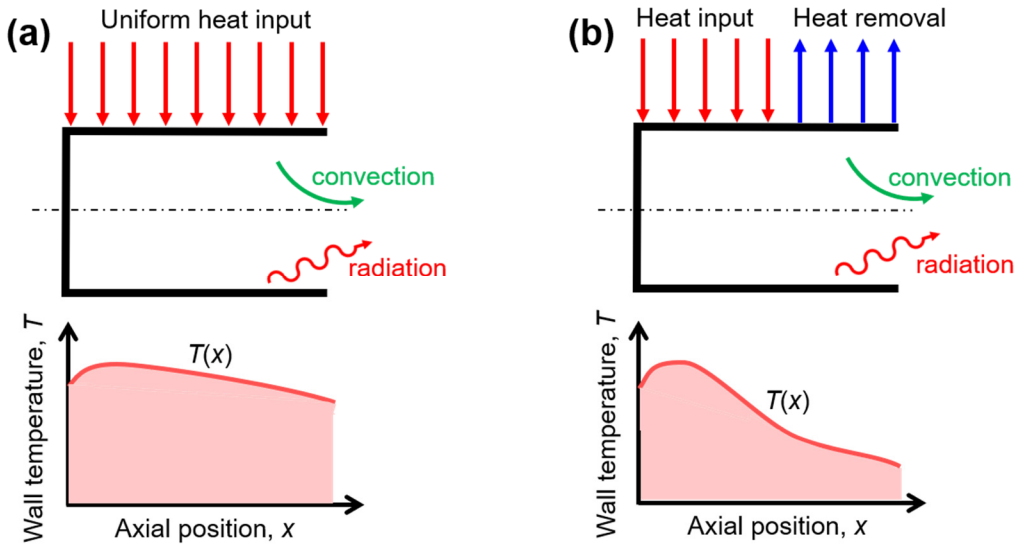

Fig. 5. Schematic representation of the rationale for using a passively-heated section to increase temperature inhomogeneity across the cavity wall. **(a)** Cavity subjected to axially-symmetric uniform heat input along its outer surface (top) and a representative wall temperature distribution $T(x)$ (bottom). **(b)** Cavity subjected to positive heat input and negative heat input (i.e. heat removal) along its different sections (top), and the resulting wall temperature distribution $T(x)$ (bottom). Note that temperature distributions shown in the schematic are merely for illustrative purposes and the reader is referred to Fig. 8(a)–(c) for plots based on experimental data. Furthermore, the radiation and convection losses through the aperture in both cases are different in magnitude.

During each experiment, the total losses of the heated cavity at steady state must be equal to the electrical power dissipated by the heating element. The dissipated power is transferred by conduction to the surrounding blanket insulation and through the cavity wall, and is thereafter convected and radiated from the cavity inner surface. An additional heat loss pathway that is considered for the AR2* cavity is heat loss via radiation and convection from the external surface of the cylindrical extension. At steady-state, the energy balance at the cavity wall is represented by Eq. (1),

$$\dot{Q}_{\text{conv}} + \dot{Q}_{\text{rad}} = P_{\text{heater}} - \dot{Q}_{\text{cond,ins}} - \dot{Q}_{\text{passive section}} , \quad (1)$$

where $\dot{Q}_{\text{conv}}$ and $\dot{Q}_{\text{rad}}$ represent the convection and radiation heat loss from the cavity aperture, respectively, P_{heater} is the input electric power as set in the Eurotherm power controller, $\dot{Q}_{\text{cond,ins}}$ is the conduction loss through the insulation surrounding the cavity and $\dot{Q}_{\text{passive section}}$ is the heat transfer from the external section of the AR2* cavity (note that $\dot{Q}_{\text{passive section}} = 0$ for AR1 and AR2 cavities). In this study, the value of convection heat loss is obtained based on the determination of conduction loss through the blanket insulation, radiation loss from the aperture and heat transfer from the passive section, as detailed in the following sections.

2.4. Estimation of conduction heat loss

The conduction heat loss through the blanket insulation as well as via other thermal pathways within the receiver casing for the AR1 and AR2 cavities was obtained experimentally by suppressing convection and radiation heat transfer from the cavity aperture with the use of a circular insulating plug, as shown in Fig. 6. The plug consisted of a Superwool insulation board with a Tombo™ Neoark ceramic cap insert (k=0.59 W/m·K at 400°C). The first step in quantifying the conduction losses through the receiver assembly for each cavity was to obtain the total power input to the respective plugged cavity for a range of average cavity temperatures and inclination angles. Internal and external temperatures of the plug, whose cross-section is shown in Fig. 6(b), were also recorded during these experiments. One-dimensional Fourier's Law was used to calculate the conduction through the plug, which was then subtracted from the total power input to obtain the conduction loss through the receiver assembly. As per its theoretical definition, the conduction loss through the receiver assembly was observed to be a function of cavity temperature. Due to the relatively small temperature difference between the receiver casing and the ambient, the magnitude of natural convection from the external surface of the receiver was neglected. The conduction loss results were then used to develop linear fits between average cavity temperature and conduction heat loss for the AR1 and AR2 cavities, as shown in Fig. 7(a). By characterising the thermal properties of the assembly surrounding each cavity in this manner, the resulting linear fits could be used in conjunction with average cavity temperatures recorded during

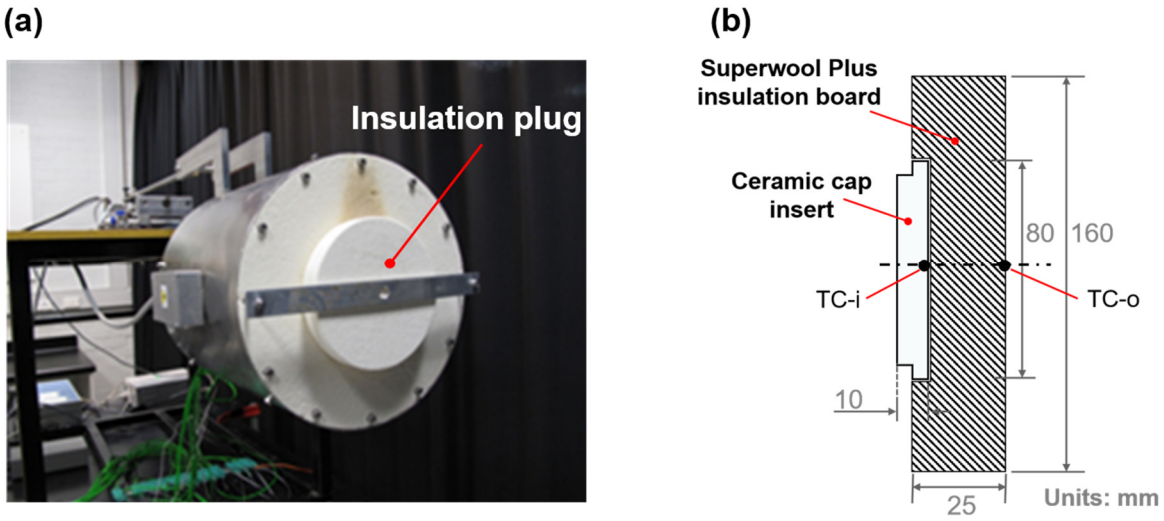

Fig. 6. Plugged cavity used to characterise conduction losses through the model receiver assembly. **(a)** Plugged cavity arrangement, showing the circular insulation plug and an aluminium bar used to keep the plug firmly in place. **(b)** Schematic of circular insulation plug, showing materials and dimensions. Also shown are the locations of thermocouples TC-i and TC-o which are used to measure the internal and external temperature of the plug, respectively.

the open-aperture experiments to obtain $\dot{Q}_{\mathrm{cond,ins}}$ for use in the energy balance represented by Eq. (1).

Based on the design of the AR2* cavity, conduction losses from the heating coil-covered section of this cavity to the blanket insulation were obtained from the fit developed for the AR1 cavity. The heat transfer from the extended section of the AR2* cavity was estimated by undertaking a similar testing regime to that of the AR1 and AR2 cavities. The plug losses and insulation losses for a range of steady-state average cavity temperatures were subtracted from the total power input, and the remainder was considered as the heat transfer rate through the external

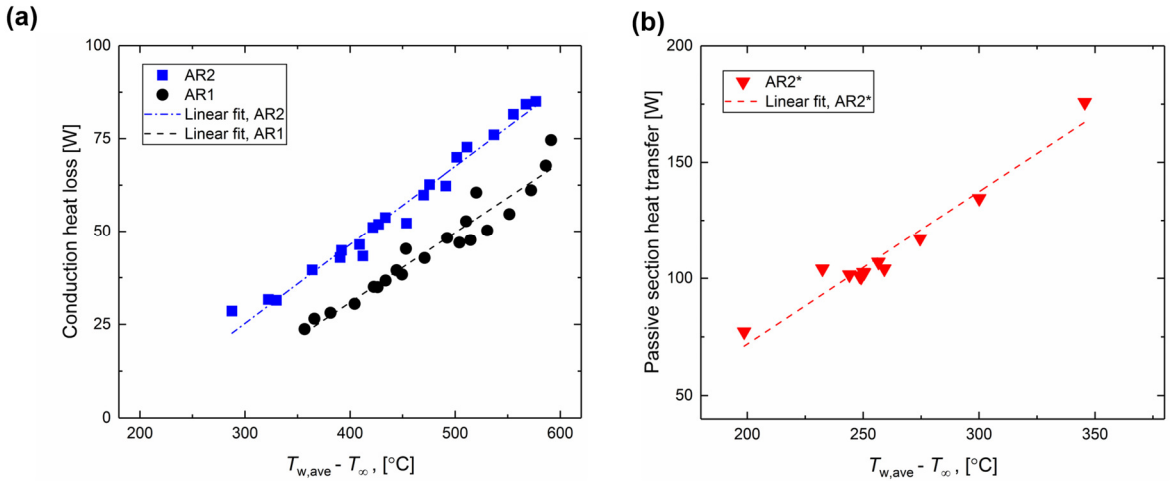

Fig. 7. Characterisation of losses from the model receiver assembly during plugged tests. **(a)** Conduction losses through the model receiver assembly, in the form of conduction through the surrounding insulation, for AR1 and AR2 cavities. **(b)** Heat transfer from the extended section of the AR2* cavity, which takes into account radiation and convection from the external surface (i.e. not though the cavity aperture). Note that the vertical axis ranges are different in these plots.

surface of the passive zone. In Fig. 7(b), data relating to the heat transfer from the extended section of the AR2* cavity is shown, as well as a linear fit to this data. By having data relating to different heat transfer pathways from the AR2* cavity, the magnitude of heat loss from the aperture of the cavity could be readily calculated.

The experimental approach used in this work to calculate losses through the surrounding insulation of the cavity takes into account conditions that might arise during the receiver assembly process, such as the presence of air gaps or thermal pathways due to compaction of insulation material or the use of structural components for positioning of the cavity within the receiver assembly; the effects of which might be difficult to accurately model. The plugged cavity approach which is used to characterise conduction losses finds frequent use in experimental convection research (Flesch, R. et al., 2015; Jilte et al., 2017; Lee et al., 2018; Torres et al., 2018; Wu, W. et al., 2014) and enables realistic consideration of the effective thermal resistance of insulation and parasitic losses within an assembly. Indeed, Jilte et al. (2017), in reporting conduction loss values based on the plugged cavity method, mentioned that the values were seemingly higher than one could expect from mere use of reported values of insulation thermal conductivity. An alternative approach for estimating conduction losses is to use a thermal resistance network model (Wu et al., 2013). This method was also used to obtain estimates of conduction loss, but the results presented discrepancies which we attribute to the inability to account for all thermal pathways in the receiver assembly.

2.5. Calculation of radiation heat loss

Calculation of radiation heat loss was undertaken analytically using the radiosity network approach (Holman, 2010) and the assumption that the wall temperature varies in the axial cavity direction. Based on a study of different discretisations of the cavity surface for the radiosity network calculation and the assumption of an average temperature for each cylindrical band—to be discussed in the following paragraphs—the assumption of axial variation of temperature was observed to be justified. This approach has previously found use in the work of McDonald (1995). With reference to Fig. 4, each node in the radiosity network was represented by a cylindrical band encompassing the thermocouples on the top and bottom section of the cavity at the same axial position. Based on this assumption, the AR1, AR2 and AR2* cavities were represented using 3, 4 and 8 nodes in the radiosity network, respectively, with an additional two nodes allocated to the aperture and back wall surface. The radiosity equation for each node is,

$$J_i = \frac{1}{1-F_{ii}(1-\varepsilon_i)}\left((1-\varepsilon_i)\sum_{j\neq i} F_{ij}J_j + \varepsilon_i E_{b_i}\right), \quad (2)$$

where J_i is the radiosity of node i, F_{ij} is the view factor between surfaces i and j, ε_i is the surface emissivity of band i and E_{bi} is the black-body emissive power of band i.

View factors for all surface-to-surface configurations were obtained by analytical relations, as specified in Howell et al. (2010). The temperature of each node in the radiosity network was assumed to equal the average temperature of thermocouples located on the top and bottom of each cylindrical band. Given that the cavity surface was coated with Pyromark-2500 paint, the total hemispherical emissivity was constrained to be between 0.86–0.88 (Ho et al., 2012).

Radiosity for each node was obtained by simultaneously solving the set of equations represented by Eq. (2) for all nodes of the radiosity network representing each cavity. The net radiation heat transfer of each node was then calculated using the following equation,

$$q_{\mathrm{rad},i} = \frac{\varepsilon_i A_i}{1-\varepsilon_i}\left(E_{b_i} - J_i\right). \quad (3)$$

The total radiation heat loss through the cavity aperture was the summation of radiative emission from the internal cavity surfaces.

The procedures used in this work for obtaining view factor values and undertaking the radiosity network analysis were verified by comparing the results with reported radiation heat loss values for cylindrical cavities of different dimensions, such as those reported in Holman (2010), Taumoefolau (2004), Jilte et al. (2013) and Wu, W. et al. (2014).

2.6. Error analysis of experimental data

Given that convection heat losses are indirectly measured using Eq. (1), the uncertainty of the convection heat loss values must be obtained by using the propagation of uncertainty in the results of the thermal losses either measured or estimated from the experimental data. In this approach, the absolute uncertainty of convection heat loss, $\delta\dot{Q}_{\mathrm{conv}}$ is calculated using Eq. (4), which is the sum of the absolute uncertainty of all terms in the energy balance analysis,

$$\delta\dot{Q}_{\mathrm{conv}} = \sqrt{(\delta P_{\mathrm{heater}})^2 + \left(\delta\dot{Q}_{\mathrm{cond}}\right)^2 + \left(\delta\dot{Q}_{\mathrm{rad}}\right)^2 + \left(\delta\dot{Q}_{\mathrm{passive\ section}}\right)^2}. \quad (4)$$

The absolute uncertainty of the measured electrical input power is considered to be $\pm(0.0025\ |P_{\mathrm{input}}|)$, given the specified accuracy of the Eurotherm power controller. Conduction losses during plugged loss experiments are directly determined with the same uncertainty as that of the electrical input power. Furthermore, as outlined in Section 2.4, the final stage of calculation of conduction loss includes the use of a linear fit of the plugged cavity test data. A maximum error of 5% for the fitted correlation is taken into account, based on data presented in Fig. 7. The total uncertainty of the conduction heat loss values is obtained by combining the power input and linear fit uncertainties using a quadratic sum, resulting in a total error of about 5.1%. The errors associated with the passive section are deemed to be equal to the conduction loss errors.

Radiation losses are determined using the radiosity network analysis, as outlined in Section 2.5. The measurement error of each thermocouple is considered to be $\pm(0.0075|\mathrm{T}|)$. As temperature is considered with the fourth power in the radiation loss calculation, the uncertainty increases at higher temperatures due to error propagation. In this work, the uncertainty in radiation loss results ranges from 10 to 20% depending on experiment conditions. It should be noted that the choice of a representative temperature for each node of the radiosity network introduces an uncertainty in the final value of radiative emission, which is different to the uncertainty due to temperature measurement error. Specifically, if either of the top or bottom thermocouple values at each axial location is used as the representative temperature for each node instead of the average of these two values, a difference of ±0.1% to ±10% can result in the value of radiation loss. This range is due to the varying temperature difference between top and bottom surfaces of the cavity at different inclinations. For the purposes of this paper, use of the average temperature is seen to be prudent and thus only the temperature measurement error is reported for the radiation loss results.

By using Eq. (4) in conjunction with the information provided above, it is found that natural convection heat loss results from experiments conducted in this study can be assigned errors ranging from 11% to 21%.

3. Results & discussion

3.1. Temperature distribution

The temperature profiles in the AR1, AR2 and AR2* cavities are shown in Fig. 8(a)-(c). A condition of constant total power at all inclination angles is set for these experiments, equal to 160 W, 150 W and 164 W for the AR1, AR2 and AR2* cavities, respectively. As described in Section 2.2, these power values result in peak temperatures in each cavity to be ~500°C at $\theta = 90°$ (downward-facing). Fig. 8(d) presents the change in the view factor of each cylindrical band along the cavity wall to the aperture. The horizontal axes show x/D, the dimensionless axial distance

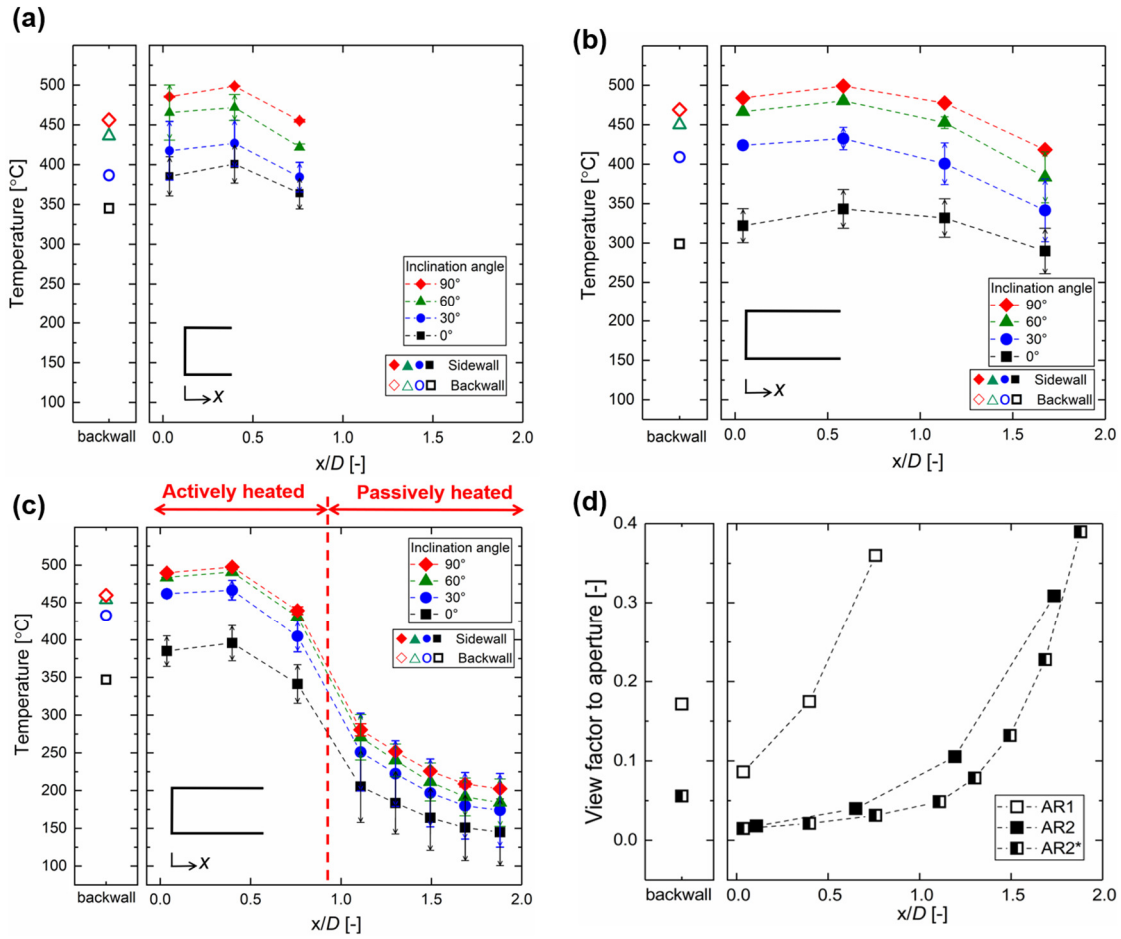

Fig. 8. Distribution of wall temperature along the wall for **(a)** AR1 **(b)** AR2, **(c)** AR2* cavities for near-constant total power input P_{heater} = 156 W (±5%). **(d)** View factor of each cylindrical band to the aperture for AR1, AR2 and AR2* cavities. Note that while x/D is measured from the cavity back wall, the left-most plot in each figure specifically shows data relating to the back wall. In parts (a), (b) and (c), each datapoint shows the average temperature at each axial position along the cavity. The bounds shown for each datapoint relate to the temperature of the top and bottom surface at the respective axial position. Experimental data that was used to produce these figures is included as Supplementary to the paper.

from the back wall. The temperature and view factor for the back wall are plotted separately in the left-most section of each part to aid visual inspection of values relating to this surface and help to distinguish these values from those relating to the thermocouples placed on the wall. In Fig. 8(a)-(c), each solid point represents the average of temperatures recorded by the thermocouples on the top and bottom surface of the cavity at the same axial location. The upper and lower range limits for each data point represent values from the top and bottom thermocouples at each axial location. The largest variation of temperatures between the bottom and top surface of the cavity is observed to be for the case of the horizontal cavity (i.e. $\theta = 0°$), in which no stagnation zone exists. The lowest such variation of temperatures is recorded for $\theta = 90°$, at which each axial location is in the same stratified layer within the stagnation zone, thereby resulting in the thermocouples in that region showing the same value.

As observed in Fig. 8(a), the wall temperature profile at all inclinations has a similar trend: the surface temperature in the vicinity of the back wall is greater than the region close to the aperture, and the highest temperature was registered by the second thermocouple from the back wall. This trend is closely associated with the smaller local view factors to the aperture, as shown in Fig. 8(d). The section located closest to the aperture has the highest view factor to the aperture, which results in the largest local radiative loss and its respective datapoint showing the lowest temperature. As x/D decreases (i.e. moving further into the cavity), the view factor to the aperture and the radiation heat loss to that surface reduces, leading to increased temperatures. On this basis, the thermocouple located closest to the back wall, at $x/D = 0.04$, would be expected to show the highest temperature. However, given that the back wall of the cavity has a larger view factor to the ambient than its adjacent wall section—see left-most plot in Fig. 8(d) —the radiative loss from the back wall is relatively higher. Furthermore, neither the back wall nor the rear-most section of each cavity in this work (refer to Fig. 4) are covered by heating coils, thus the energy loss due to radiation is not compensated and, in all three cavities, a lower temperature is recorded at $x/D = 0.04$ in comparison to the temperature recorded by the second thermocouple from the backwall. In this regard, similar qualitative observations have been reported by Wu et al. (2013) and Wu, W. et al. (2014).

An indication of the influence of convective losses on cavity temperature distribution can be obtained by a more detailed examination of Fig. 8(a)–(c). Firstly, the increase in average cavity temperature with inclination angle at a given location can be attributed to an increasing volume of stagnant hot air within each cavity. As hypothesised by Clausing (1981), a stagnant volume of heated air forms above a horizontal free-shear plane which intersects the cavity at the top of the aperture lip; this bounded volume increases with the inclination angle of the cavity. The surface area below the horizontal plane, termed the convective zone, contributes to the direct removal of heat from the cavity by way of convection.

Secondly, convection causes a departure from axial symmetry of the temperature profile. At $\theta = 90°$, the stagnation zone is essentially a stratified volume of hot air occupying the entire cavity and thus, is at its maximum value. As can be seen in the data for all three cavities at $\theta = 90°$, the thermocouples at each axial location show no variation between top and bottom wall temperature values, representing a quasi-isothermal condition. At this inclination, although stratification occurs within the cavity, convection is still present near the aperture, similar to the case of a downward-facing heated surface. The characteristic length definition used in the

538 convective zone definition proposed by Clausing ensures that the estimated convection heat loss
539 at $\theta = 90°$ is a non-zero value, as shown in the experimental results presented here and previously
540 reported by Taumoefolau et al. (2004). When the cavity is inclined at angles $\theta < 90°$, the convection
541 zone develops. As seen in Fig. 8(a)-(c), two trends in the data for $\theta = 60°$ and $\theta = 30°$, signify the
542 presence of the convection zone: first, a decrease of average cavity temperature, and second, the
543 larger temperature bounds at the locations of each thermocouple in all three cavities, as compared
544 with the respective datapoints at $\theta = 90°$. As an example, in Fig. 8(b) which relates to the AR2
545 cavity, at $\theta = 30°$ the thermocouples located along the bottom wall at $x/D = 1.1$ and $x/D = 1.7$
546 are in the convective zone, and hence the temperature of the air as it flows across the bottom
547 surface is noticeably different to its temperature at the top wall, and thus the wall temperature
548 bounds are larger. In contrast, in the same cavity and at $\theta = 60°$, more than half of the cavity
549 volume is taken up by the stagnant zone, evidenced by the smaller temperature bounds for each
550 axial location compared to $\theta = 30°$. At all axial positions along the cavity at the horizontal
551 orientation ($\theta = 0°$), a larger temperature difference exists between the top and bottom wall, as
552 represented by the upper and lower limit of each datapoint. At this orientation, ambient air enters
553 the cavity from the lower portion of the aperture and cools the bottom surface of the cavity. At
554 this inclination, no stagnation zone exists and the air entering the cavity gradually rises in
555 temperature as it flows across the cavity surface. The increase in the temperature of the air results
556 in its increased buoyancy, giving rise to an upward flow particularly strong near the back wall of
557 the cavity. The heated air then leaves from the upper portion of the aperture, as previously
558 visualised in the experimental studies by Chen et al. (1985) and Yeh et al. (2005).
559 Fig. 8(c) shows the temperature distribution for the AR2* cavity. For this cavity, $x/D <$
560 0.8 represents the section of the cavity exposed to heating coils, while $1 < x/D < 2$ is the passively
561 heated section. The actively-heated section of the AR2* cavity exhibits qualitatively similar
562 temperature profiles to the AR1 and AR2 cavities over the range of inclination angles. For example,
563 with an increase in inclination angle, the ever-increasing stagnant zone results in reduced
564 temperature difference between the top and bottom walls. Given that the extended section of the
565 AR2* cavity is exposed to external convection and radiation in addition to convection and
566 radiation loss from the aperture, a larger reduction in temperature is recorded near the aperture,
567 in comparison to the AR2 cavity.
568 Comparison of the temperature distribution in the three cavities at all inclination angles
569 shows a significantly larger variation of temperature along the wall of the AR2* cavity than for the
570 other two cavities. The implications of the temperature distribution in the cavities—which
571 emanates from their different heating arrangements and geometric aspect ratio—is discussed in
572 more detail in the following sections.
573
574 *3.2. Breakdown of thermal loss components*

575 Fig. 9 shows the breakdown of heat loss components from the AR1, AR2 and AR2*
576 cavities as a function of the inclination angle for near-constant total power input of 156 W (±5%),
577 corresponding to the temperature profiles in Fig. 8. Detailed data which, among other things,
578 includes surface temperatures of the convection and stagnation zone, is presented in the Appendix
579 of this article as Table A1 and is used to analyse the trends seen in Fig. 9. As previously discussed,

with the change in inclination angle from $\theta = 0°$ to $\theta = 90°$, the average temperature in the cavity increases due to the increasing stagnation zone within the cavity. Data relating to convection heat loss is presented in Fig. 9(a) and shows that for all three cavities, the overall trend of change in convection loss as inclination changes from $\theta = 0°$ to $\theta = 90°$ is one of reduction. This can be attributed to the increasing size of the stagnation zone, or conversely the reduction in size of the convective zone A_{cz}, as cavity inclination is increased. Note that for the purposes of this work, convective zone surface area A_{cz} is defined as the summation of the full aperture area and the lateral and back wall surface areas below the horizontal free-shear layer. On this basis, for all three cavities, the maximum convection loss occurs at $\theta = 0°$ while the minimum occurs at $\theta = 90°$, i.e. the bounds of inclination angle ranges considered in this study. Comparison of the data relating to the three cavities shows that at $\theta = 0°$, the AR2 and AR2* cavities have higher convection loss which is due to the larger surface area of the cavities constituting the convective zone. However, the large surface area becomes less important as the cavity is inclined, due to the diminishing ratio of convective zone surface area to the total cavity wall surface area A_{cz}/A_w (see Table A1). For example, at $\theta = 30°$ and $\theta = 60°$, the AR1 cavity has a convective zone surface area A_{cz} that is smaller than or equal in size to the two other cavities; however on a proportional basis, this zone encompasses a larger fraction of the total surface area (i.e. larger A_{cz}/A_w) in the AR1 cavity than it does in either of the AR2 or AR2* cavities. Furthermore, given that the average temperature of the convective zone surface in the AR1 cavity is higher than the respective temperature in the AR2 and AR2* cavities, this contributes to the larger convection loss in the AR1 cavity. In contrast, comparison between the AR2 and AR2* cavities shows that despite both having the same A_{cz} and A_{cz}/A_w, the AR2 cavity has higher convection losses than the AR2* cavity due to the higher surface temperature in its respective convective zone. At $\theta = 90°$, A_{cz} is equal to the aperture surface area, which is the same for all cavities. Convection at this inclination can be considered as natural convection from a horizontal downward facing heated surface. Due to there being higher bulk air temperatures closer to the cavity aperture in the AR1 cavity, this cavity exhibits a higher convection loss. The AR2 and AR2* cavities benefit from a larger stagnant zone, leading to a temperature stratified cavity interior with the coolest zone close to the aperture; this effect is instrumental in their lower convection loss at this downward angle.

In Figure 9(b), the overall trend of increasing radiation heat loss from the three cavities as inclination changes from $\theta = 0°$ to $\theta = 90°$ can be attributed to the increase in average cavity temperature. It can also be seen that the influence of a significant reduction in wall temperatures towards the aperture in the AR2* cavity results in a substantial reduction of radiation heat loss, as compared to the AR2 cavity. In the case of the AR2* cavity, the average temperature of the heated section is higher than the other two cavities, but its respective radiation loss value is significantly lower because of the lower view factor to the ambient of the cavity sections at higher temperature.

Fig. 9(c) presents the data relating to conduction within the receiver assembly for the three cavities. Additionally, to provide a complete picture of the thermal loss pathways within the experiment, the parasitic losses from the AR2* passive section are also presented in the plot. With reference to Fig. 3(b), it can be seen that the AR1 and AR2* cavities have the same heated area which is exposed to insulation. At $\theta = 0°$, 75° and 90° where the temperature of the heated section of the two cavities is similar, the conduction losses are also seen to be equal. However, at other inclination angles where the convective zone dynamics result in different heated section

623 temperatures, the conduction losses also vary. Conduction losses from the AR2 cavity, which is
624 heated and covered by insulation along its full length, are seen to be greater than the two other
625 cavities. As cavity inclination increases, the temperature within the AR2* cavity also increases,
626 leading to increased wall temperatures in the passive section. This results in increased radiation
627 and convection loss from the external surface of the passive section.
628 A similar thermal loss analysis has been undertaken for the three cavities when the peak
629 temperature in each cavity is kept constant at ~500°C for inclination angles ranging from $\theta = 0°$
630 to $\theta = 90°$. For the sake of brevity, the graph is not presented here, but is included as part of
631 Appendix A (Fig. A1 and Table A2) for interested readers. Despite the different temperature
632 conditions along the cavity wall between the two approaches used here—as detailed in Section
633 2.2—the trends observed in convection losses are similar. Given that average cavity temperature
634 varied by only 20°C across the full span of inclination angles when the peak temperature in the
635 cavity was kept constant, the radiation and conduction losses were essentially constant. Radiation
636 losses for the AR2* cavity reduced by close to 60% in comparison to the AR1 and AR2 cavities.
637 Results presented in Fig. 9 and Fig A1 as well as data in Tables A1–A2 provide a detailed
638 understanding of the changes in thermal losses, especially that of convection heat loss, at different
639 cavity inclinations. They highlight that understanding the influence of the convective zone surface
640 area and cavity temperature variations is necessary when discussing trends in convection losses
641 from cavities that have non-isothermal temperature distributions. These insights are utilized in the
642 analysis which underpins the correlation that is proposed in this work, as explained in Section 4.

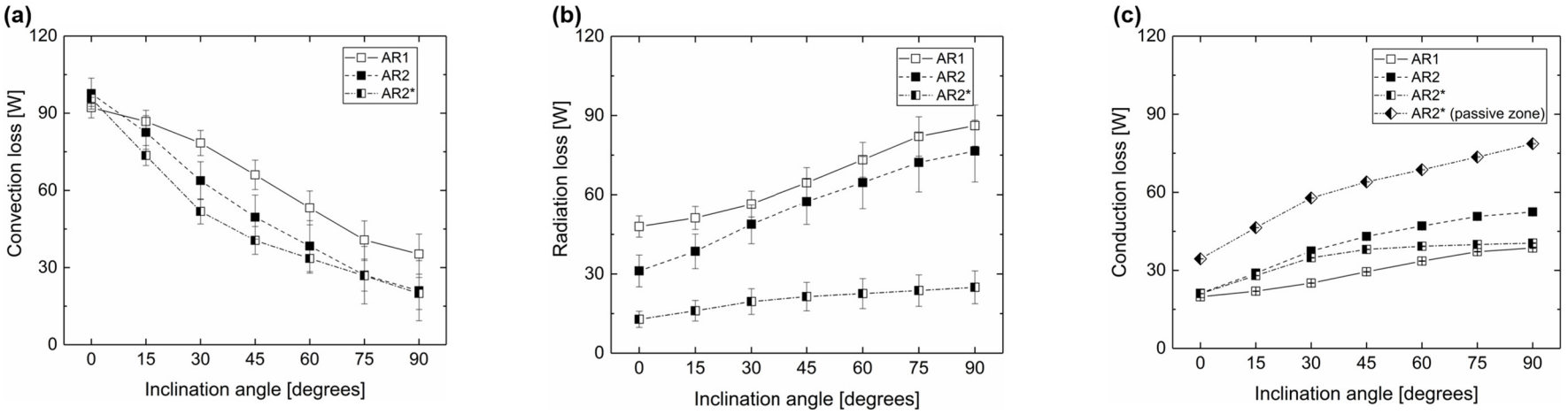

Fig. 9. Breakdown of thermal losses, including error bars, for experiments with near-constant total power input, P_{heater} = 156 W (±5%). **(a)** Convection loss, **(b)** Radiation loss, **(c)** Conduction loss, including passive section heat loss. Corresponding temperature profiles are shown in Fig. 8.

Fig. 10 presents the ratio of convection to the total heat loss through the cavity aperture $\dot{Q}_{conv}/\dot{Q}_{ap}$ as a function of inclination, for a number of different cavity peak temperatures. The data is obtained from experiments undertaken using the AR1 cavity, whereby a constant peak temperature was maintained in the cavity across the full range of receiver inclination angles. In these experiments, the average cavity temperature across the span of inclination angles varied by only ~20°C. The proportion of convection heat loss from cavity aperture is observed to decrease with increasing temperature, whereas the balance, i.e. radiation leaving the aperture, increases. This behaviour can be attributed to the dependence of radiation to the fourth power of absolute temperature being stronger in a relative sense than that of convection which is dependent on a lower power of the temperature difference. For instance, in the case of 650°C peak temperature, for $\theta \geq 0°$, the majority of the energy lost through the aperture can be attributed to radiation. However, for the case of 495°C peak temperature, convection heat loss is the major mechanism of heat loss only at inclination angles $\theta \leq 45°$. A similar experimental result was reported by Lee et al. (2018), albeit at a single inclination angle of $\theta = 15°$.

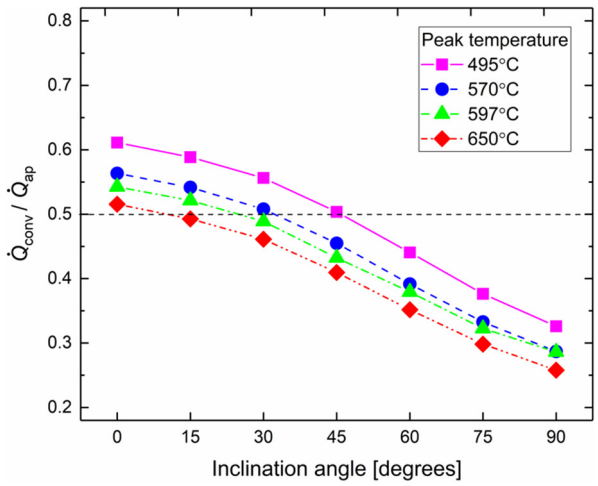

Fig. 10. Change in ratio of convection heat loss to total heat loss (i.e. convection + radiation) through cavity aperture as a function of inclination angle, at various cavity peak temperatures for AR1 cavity. Note that the average cavity temperature for each curve varies by no more than 20°C across the full range of inclination angles.

3.3. Comparison of experimental convection loss results with estimates obtained from Nusselt correlations

Fig. 11 provides a comparison between natural convection heat loss results from experiments undertaken in the present work with estimates obtained from the use of relevant correlations from the literature. Area-averaged cavity temperatures from the experimental data are taken as representative cavity temperatures for use in these correlations, all of which assume isothermal boundary conditions. Results obtained from the use of the correlation proposed in this work, which will be discussed in greater detail in Section 4, are also presented in this figure for comparative purposes.

In general, most correlations predict a decreasing trend for convection loss as a function of cavity inclination, with the highest value predicted for a horizontal cavity, $\theta = 0°$ and the lowest value for a downward-facing cavity, $\theta = 90°$. However, a number of correlations exhibit systematic

discrepancies at certain inclination angles that detract from their efficacy to predict the experimental data and trends obtained in this study.

The correlation proposed by Clausing et al. (1987) has become a gold-standard as a predictive tool for estimating convection loss for different cavity geometries. This correlation is observed to provide accurate predictions of the experimental convection losses of the present work. However, the complex nature of the formulation and the iterative calculation of one of its parameters presents opportunities for the development of simpler correlations that can capture the subtleties observed from specific experimental data and cavity geometries. On this basis, Section 4 provides a correlation which not only predicts values within similar error bounds as Clausing, but at times provides more accurate predictions, as clearly seen in Fig. 11.

The correlation proposed by Koenig and Marvin as reported in (Harris and Lenz, 1985), as well as those of Stine and McDonald (1989) and Jilte et al. (2017) predict somewhat increased losses at $\theta = 15°$ in comparison to $\theta = 0°$ for the AR2 and AR2* cavities. Calculations not presented here have shown that if isothermal conditions are maintained across all cavity inclinations, this increasing trend of losses at $\theta = 15°$ is not observed. In the case of a non-isothermal AR1 cavity, the increase in average cavity temperature from an inclination of $\theta = 0°$ to $\theta = 15°$ (~11°C) is balanced by a factor which considers the change in inclination. However, in the case of the AR2 and AR2* cavities, this temperature difference is approximately 45°C and the cavity inclination factor does not reduce the convection loss value.

The correlation proposed by Leibfried and Ortjohann (1995) is a modification of the Stine and McDonald (1989) correlation. It includes a revised factor for the consideration of the influence of geometry on air flow inside the cavity, as well as a more complex cavity inclination factor which considers upward and downward-facing cavities. The former parameter ensures that for AR1 and AR2 cavities, the different magnitude of surface areas are taken into account, whereas the original Stine and McDonald (1989) correlation only takes into account the ratio of cavity diameter to aperture diameter, which stays the same for the three cavities of this study. In effect, the two revised factors of the Leibfried and Ortjohann (1995) correlation allow for improved estimates of the convection loss in comparison to the correlation of Stine and McDonald (1989).

The correlation by Paitoonsurikarn et al. (2011) uses a characteristic length definition in the *Ra* and *Nu* formulations with the intention of foregoing the complex calculations relating to convective zone surface areas for different cavity geometries at various inclination angles. While this objective is certainly met, the definition of this *ensemble length* is based on constant parameters obtained from three cavity geometries. Furthermore, given that the characteristic length definition results in negative values in the case of large aspect ratio cavities at high inclination angles, using the absolute value in such cases has been suggested. Given these conditions, it seems that the ensemble length cannot be considered as an accurate and general characteristic length definition for different geometries. In fact, the current experimental results as well as convection loss results of other studies in the literature, e.g. (Wu, W. et al., 2014), (Uhlig et al., 2014) and (Samanes et al., 2015), have either been under- or over-predicted to a large degree by this correlation.

A numerical study by Jilte et al. (2013) resulted in a correlation based on A_{ib}, the inclination-dependent surface area encompassing lateral surfaces below the stagnation plane and the surface area of the shear layer between the stagnant zone and convective zone. The correlation which is used in Fig. 11 is obtained from isothermal cavity experiments reported by Jilte et al. (2017) that

resulted in findings showing the aperture area to be better suited for the prediction of losses. However, as was stated before, this correlation predicts increased losses from $\theta = 0°$ to $\theta = 15°$. The performance of the latter correlation has been observed to be slightly worse than the correlation earlier proposed by Jilte.

Another observation that can be made regarding Fig. 11 is that the correlation by Koenig and Marvin (Harris and Lenz, 1985), Stine and McDonald (1989) and Leibfried and Ortjohann (1995) predict a zero value of convection loss at $\theta = 90°$ which does not seem plausible. The selection of suitable factors for cavity inclination ensures that the other correlations presented here better predict losses at higher inclination angles.

It should be noted that two relevant natural convection correlations that were proposed by Prakash (2014) and Wu et al. (2013)—the latter considering a flux-based Grashof number—were also used but the predictions were not more accurate than the correlations used here. As such, these results are not presented here.

In summary, it seems that in order to estimate convective losses from non-isothermal cavities, it is important to consider the changing magnitude of surface areas which influence convection heat loss. As previously mentioned, mere use of a representative cavity temperature without alluding to the changing magnitude of convective zone surface area at different inclinations causes errors in the estimates. Furthermore, suitable cavity inclination factors are needed to ensure the prediction of non-zero convection loss at $\theta = 90°$.

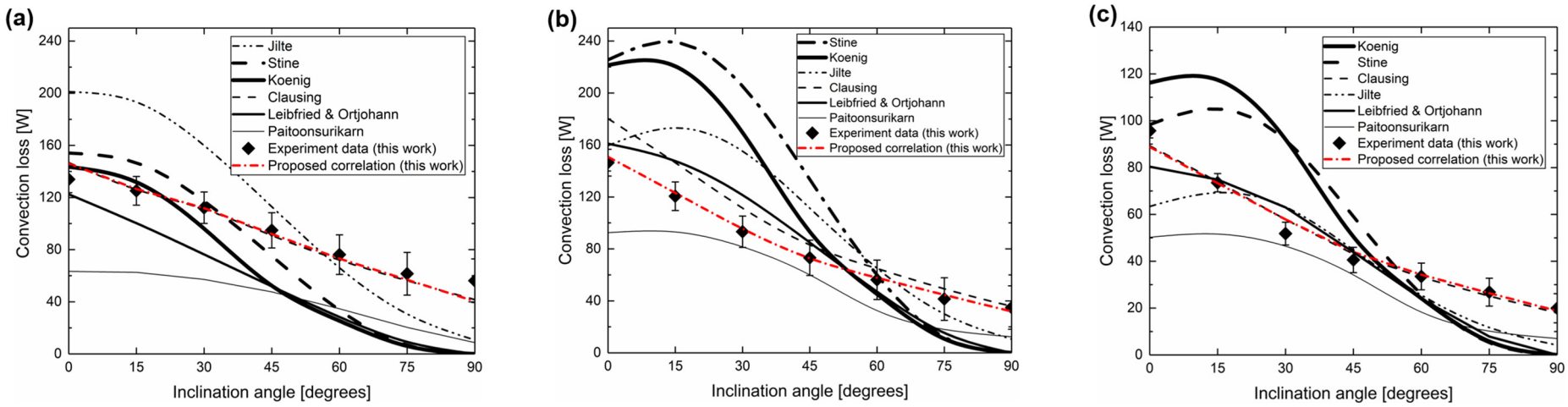

Fig. 11. Comparison of experimentally-derived natural convection heat loss results from the present work (solid points) with estimates provided by correlations in the literature and a new proposed correlation (explained in detail in Section 4). Experimental data relate to the cases of **(a)** AR1 cavity, P_{heater} = 294 W, **(b)** AR2 cavity, P_{heater} = 275 W, **(c)** AR2* cavity, P_{heater} = 164 W. Details of the reference for each correlation cited in the legend are as follows: Koenig (Harris and Lenz, 1985); Clausing (Clausing et al., 1987); Stine (Stine and McDonald, 1989); Leibfried & Ortjohann (also known as mod. Stine) (Leibfried and Ortjohann, 1995); Paitoonsurikarn (Paitoonsurikarn et al., 2011); Jilte (Jilte et al., 2017).

4. Nusselt number correlation for convection loss

4.1. Discussion of parameters influencing convection heat loss in a non-isothermal cavity

Based on the evaluation which was undertaken in Section 3.3, it was observed that correlations other than Clausing predicted experimentally-derived convection loss values with varying degrees of accuracy. In some cases, the magnitude of convection loss was incorrectly estimated and in other cases, the trends defied the observed patterns in the data. For this reason, an investigation was undertaken to examine parameters for a new Nusselt correlation which could predict the trends in the data with more accuracy. In this endeavour, findings obtained from the analysis undertaken in Section 3.2 regarding influential parameters on convection loss were taken into account.

A review of natural convection correlations which have been proposed from 1980 to 2010, as summarised by Wu (2010), and since then by subsequent publications, shows that most empirical correlations consider factors relating to the Grashof number, cavity inclination and geometry, as shown in Eq. (5).

$$Nu = f_1\left(Gr_{L_c}\right) \cdot f_2(\theta) \cdot f_3(Geometry), \tag{5}$$

where each factor on the right-hand side represents a dimensionless function, which considers the influence of the referenced parameter.

In formulating a revised version of the Nusselt correlation, a number of considerations were taken into account regarding the form of the functions in Eq. (5), as described below:

Grashof number, Gr: The temperature-based definition of the Grashof number *Gr*, rather than the flux-based definition, will be used due to the practicality of obtaining temperature data from experiments. The decision to define the proposed correlation based on *Gr*, rather than the Rayleigh number $Ra = Gr \cdot Pr$, is due to the Prandtl number *Pr* being essentially a constant, 0.7, in the laboratory environment conditions encountered in our work, which has restricted any evaluation of functional dependence for *Pr*.

Characteristic length, L_c: Based on conventions in the literature, cavity diameter *D* and cavity length *L* were considered as two possible candidates for the characteristic length parameter used in the definition of the Grashof number and for subsequent use in the calculation of convection heat loss. Following the convention used in the work of Clausing et al. (1987)—where the author reasoned that this definition allowed for the best correlation of the experimental data—the vertical projection of the aperture diameter plus one-half of the internal dimension of the cavity, $D_{ap,\perp} + L/2$ was also considered. However, the length definition proposed by Clausing was based on experiments undertaken with a cubical cavity. Given that a cylindrical cavity was used in the current work, an alternative to the Clausing definition was considered, which is the vertical projection of the aperture diameter plus one-half of the aperture diameter, $D_{ap,\perp} + D_{ap}/2$. This definition ensures that the height of the aperture is taken into account at all inclinations $\theta \neq 90°$. For the case of $\theta = 90°$, the term $D_{ap}/2$ results in a non-zero value for Grashof number. Selection of the aperture radius, while mainly based on the convention set by Clausing, has previously been found to adequately represent the characteristic length relating to natural convection from the bottom of round heated surfaces (Faw and Dullforce, 1982; Radziemska and Lewandowski, 2001).

Cavity inclination, θ: Two different formulations for the functional dependence on cavity inclination were considered. The parameter most widely used in the literature is $(1+\cos\theta)$. However, results presented in Section 3.2 showed that the ratio of convective zone to total wall area A_{cz}/A_w could be more descriptive of the changing dynamics of convection loss at different cavity inclinations than the simplistic $(1+\cos\theta)$ factor which results in the same value for all cavity shapes and sizes.

Geometry: Given that cylindrical cavities of two different aspect ratios L/D were used in the current work, the effect of inclusion or omission of this parameter in the proposed correlation was studied.

Temperature non-uniformity: The novel contribution of the present work relates to its consideration of the temperature non-uniformity within a cavity in the formulation of a proposed Nusselt correlation. To appropriately account for the effect of cavity temperature non-uniformity, four candidate definitions were initially considered, with one of the candidates subsequently being omitted. The factor most widely used in the literature to account for the influence of variable air properties at elevated temperatures within a cavity is T_w/T_∞ (Clausing and Kempka, 1981; Siebers et al., 1985). The inclusion of this factor as a candidate in the formulation of the correlation was to check whether it would be useful in explaining the trends observed in the non-isothermal cavity of the present experimental work. Nonetheless, given the wall temperature distribution encountered in the present work, other temperature definitions that could represent the temperature variation along the cavity wall were also formulated for consideration. The first alternative candidate for this parameter was the *temperature non-uniformity index* defined as $T_{w,ave}/(T_{w,x=L}-T_{w,x=0})$ by Najafabadi and Ozalp (2018). For an ideal isothermal cavity, this index approaches infinity and as such, accounting for its large values would be difficult in a correlation. For this purpose, neither this factor nor its reciprocal was considered. Instead, T_{max}/T_{min} and $(T_{max}-T_\infty)/(T_{min}-T_\infty)$ were considered for further investigation. The usefulness of these two definitions is due to their approaching a value of 1 for an isothermal cavity and values larger than that for non-isothermal cavities.

4.2. Proposed Nusselt number correlation for convection loss

A total of 48 combinations of the parameters described above were considered for the formulation of Eq. (5). Each form of the Nusselt correlation was investigated by comparing it to experimentally-derived Nusselt numbers and obtaining exponent values for each parameter function using the Levenberg-Marquardt algorithm (Morge, 1978) for non-linear regression. The resulting correlations were assessed in terms of statistics of fit and the appropriateness of the exponents. The latter criterion was used due to some combinations of functional relationships resulting in negative exponents for factors such as *Gr* which was in conflict with previously reported trends in the literature. Once a reduced list of candidate combinations was obtained, the Nusselt number correlation which produced the most accurate estimate of experimentally-derived convection heat loss was chosen. This correlation is represented by Eq. (6).

$$Nu = 0.126\, Gr_{L_c}{}^{1/3}\ (T^*)^{0.11} AR^{-0.52} \left(\frac{A_{cz}}{A_w}\right)^{0.80}, \quad (6)$$

where $Gr = \frac{g\beta(T_{ave,cav}-T_\infty)L_C^3}{v^2}$, $L_c = D_{ap,\perp} + D_{ap}/2$, $T^* = \frac{T_{max}-T_\infty}{T_{min}-T_\infty}$ and $AR = \frac{L}{D}$.

The Nusselt number obtained from Eq. (6) can be used with the following equation to obtain the natural convection heat loss from the cavity.

$$\dot{Q}_{conv} = \frac{Nu \cdot k_f}{L_c} A_w (T_{ave,cav} - T_\infty). \quad (7)$$

In Eq. (6), A_w is the total wall area of the cavity, equal to the summation of the lateral and back wall surface areas of the cavity. The convective zone surface area A_{cz} is the summation of the total aperture area as well as the lateral and back wall cavity surface areas below the horizontal free-shear layer. Fig. 12 presents a schematic showing the stagnation and convection zones in an inclined cavity, which can inform the process of calculating A_{cz}. Thermophysical properties that are used for *Gr* and subsequent derivation of $\dot{Q}_{conv}$ are evaluated at the film temperature which is defined as $T_f = (T_{ave,cav} + T_\infty)/2$.

The experimental datasets used in the development of Eq. (6) originate from four sources, namely experimental data acquired as part of the present work, as well as data reported by Taumoefolau (2004), Wu, W. et al. (2014) and Jilte et al. (2017). These four datasets explicitly relate to cylindrical cavities. Parameters which describe the specifications of each dataset are presented in Table 1.

During the initial regression analysis, the exponent of the Grashof number was unconstrained, and values between 0.31–0.35 were obtained for many of the candidate correlations. For the initial form of Eq. (6), the regression analysis resulted in a value of 0.34 for the exponent of *Gr*. Given that an exponent of 1/3 is widely used in the literature for this parameter, it was decided to constrain this value to 1/3 and repeat the regression analysis to obtain updated exponents for the other parameters in the correlation.

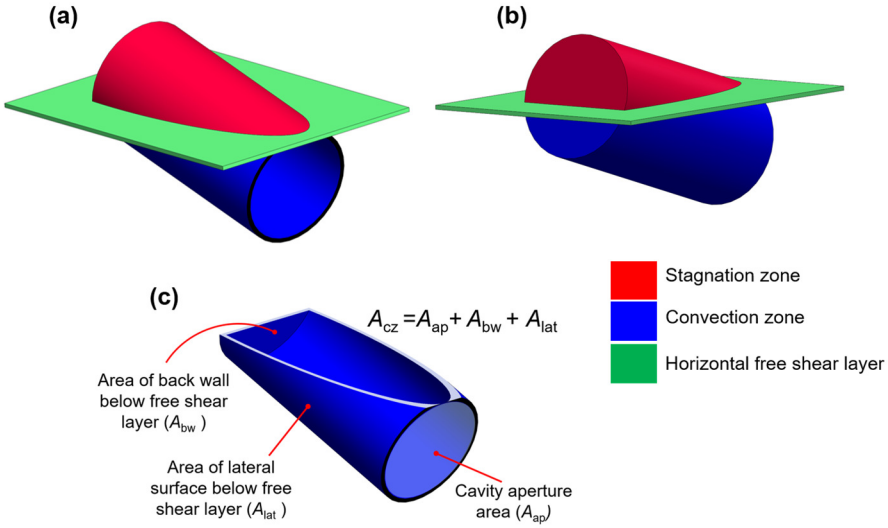

Fig. 12. Stagnation (red) and convection (blue) zones for an inclined cylindrical cavity. (a) Isometric front view, showing horizontal free-shear layer intersecting cavity at top of aperture. (b) Isometric rear view, showing segments of the back wall in stagnation and convection zones. (c) An example calculation of A_{cz} using its constitutive inclination-based areas for use in correlation Eq. (6).

Table 1. Specification of experimental cylindrical cavity datasets used in the development of the correlation proposed in this study, Eq. (6)

Dataset	Data points	L/D [mm/mm]	AR	Temperature [°C]	T^*	Gr
Present work	84	83/83 166/83	1 2	355 – 653	1.10–3.85	2.63×10^5–1.36×10^7
(Taumoefolau, 2004)	15	156/70	2.14	450, 550, 650	1.03–1.07	1.50×10^5–4.98×10^6
(Jilte et al., 2017)	7	255/149	1.71	225, 325, 425	1.07–1.13	2.27×10^6–8.41×10^7
(Wu, W. et al., 2014)	3	245/158	1.56	400, 600, 800	1.28–1.30	4.67×10^6–3.19×10^6

The presence of the exponent of $1/3$ for the Grashof number when it is used to calculate the convection heat loss will result in the characteristic length term being cancelled out and seemingly rendering the choice of any specific characteristic length definition as immaterial in the final analysis. A comparison of the parity plots for convection heat loss based on different candidate correlations when either D or $D_{ap,\perp} + D_{ap}/2$ is used shows that this is not the case. The reason is that the choice of L_c influences the value of Gr in the regression analysis, and thereby the exponents of other parameters in the correlation will also change. A case in point is when T_w/T_∞ is used as the temperature non-uniformity function in Eq. (5), in conjunction with two different characteristic length definitions. Fig. 13 shows this comparison, whereby the correlation incorporating the cavity diameter as the characteristic length consistently overpredicts the experimental losses by 30%. The analysis undertaken as part of refinement of the proposed correlation resulted in the selection of characteristic length equal to $D_{ap,\perp} + D_{ap}/2$ and the temperature non-uniformity factor $T^* = (T_{\max} - T_\infty)/(T_{\min} - T_\infty)$ as the optimal parameters to predict convection loss.

The dimensionless temperature factor defined as $(T_{\max} - T_\infty)/(T_{\min} - T_\infty)$ in the proposed correlation takes into account the minimum and maximum temperatures recorded in the cavity at

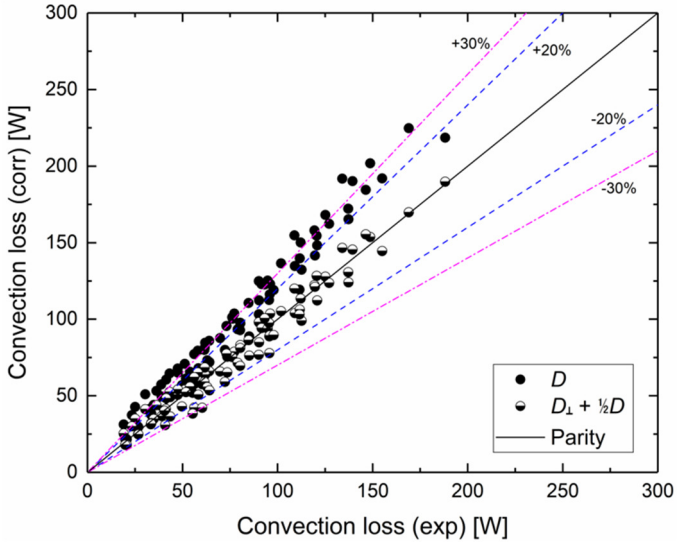

Fig. 13. Convection heat loss parity plots showing the difference arising from use of two different characteristic length definitions, and T_w/T_∞ as the candidate temperature non-uniformity function

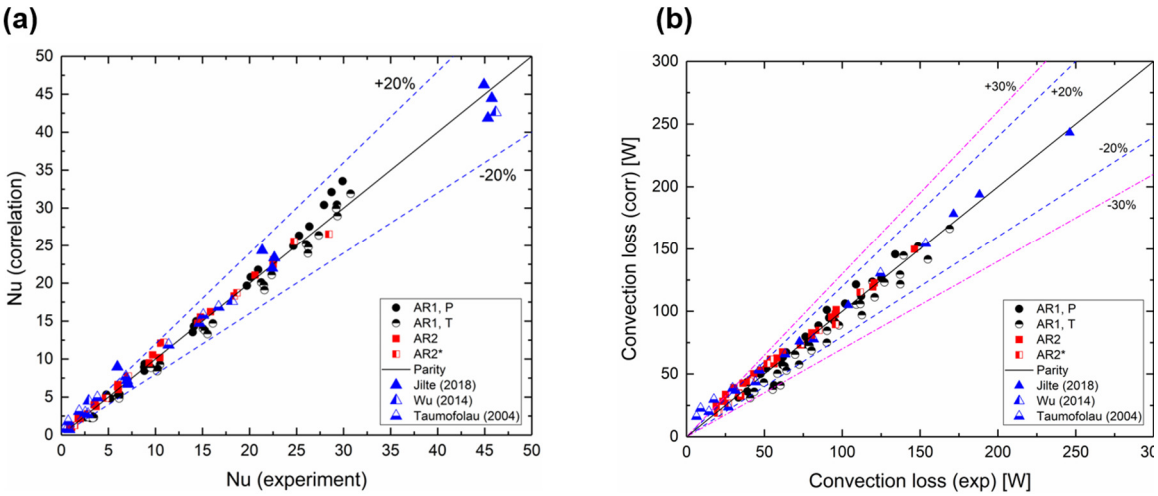

Fig. 14. Parity plots for the correlation represented by Eq. (6), utilising the temperature non-uniformity factor T^* and datasets outlined in Table 1. **(a)** Nusselt number parity plot; **(b)** Convection heat loss parity plot.

steady-state conditions. The major underlying assumption in the definition of this factor is that the region with the highest temperature is situated towards the back of the cavity and the lowest temperature is observed towards the front of the cavity, in proximity to the aperture. Values of this temperature factor ranged from 1.10 to 3.85 for data obtained from experiments conducted as part of this work, with the upper limit of this range being attributable to results obtained from the AR2* cavity. The only dataset used in the development of the correlation which is claimed to be isothermal, thus having $T^* = 1$, is that of Jilte et al. (2017). However, based on their reported data, the actual value of T^* varies between 1.07 to 1.13. Accordingly, these latter values were used to ensure accurate representation of data during the development of the correlation. Inclusion of T^* in the correlation has been observed to improve the estimate of convection loss by between 2 and 15%. The analysis underpinning the development of this correlation shows that inclusion of the T^* factor results in reduced standard deviation and residual sum of squares in the fitting process, as compared to the case when T^* is not used. Furthermore, the Wald test undertaken on this factor shows it to be statistically significant. Results of the regression analysis carried out for the correlation represented by Eq. (6) are included in Appendix B.

The functional dependence on aspect ratio is observed to have a negative exponent, signifying that for longer cavities, the Nusselt number will decrease. This result is based on trends obtained from the experimental data of this work, which considers the effect of a non-isothermal temperature distribution. A numerical study by Lee et al. (2017) which investigated the influence of aspect ratio on cavity heat loss determined that an increase in aspect ratio would result in higher convection losses for an isothermal cavity. However, Lee et al. (2017) further cautions on extrapolating the finding to non-isothermal cavities. The results presented here, and more specifically in Table A2, highlight the prudence of that statement and reiterate the importance of considering temperature non-uniformity effects in cavities.

Fig. 14 shows a comparison between the Nusselt number and convection loss results obtained from experiments and from the proposed correlation, Eq. (6). Fig. 14(a) shows the Nusselt number parity plot for the combined dataset, while Fig. 14(b) shows the convection loss

parity plot. The proposed correlation predicts 85% of data within ±20% deviation and 92% of data within ±30% deviation.

4.3. *Comments regarding the use of the correlation proposed in this work*

The proposed correlation represented by Eq. (6) uses the T^* factor, for which an a priori estimate of the temperature distribution in a receiver is required. An iterative energy analysis process, which is routinely undertaken in the design and analysis of solar thermal receivers, can be used to obtain the required surface temperature distribution. In this approach, radiative emission and convection losses from the receiver surface as well as the hydrodynamic performance of the heat transfer fluid in the receiver tubes are considered to be the main drivers of steady-state values of receiver temperature. Even though a description of the energy analysis process will be provided here for the sake of completeness, a detailed investigation is out of the scope of the current work and interested readers are referred to other published work in the literature, e.g. (Cagnoli et al., 2017; Lin et al., 2018; Pye et al., 2015; Tu et al., 2013), for more details.

Fig. 15 presents a high-level schematic of the steps that can be taken to obtain the temperature distribution in a solar receiver. Initially, optical ray tracing models can be used to obtain the distribution of solar flux from the concentrator surface at the cavity aperture plane or onto the absorber tube surfaces (Asselineau et al., 2015; Wang et al., 2018). Selection of constants such as cavity surface emissivity ε, as well as the initial distribution of surface temperature and convection heat transfer coefficient h enables the calculation of an initial value for radiative emission and external convection from the receiver surface. These heat loss values can then be used in conjunction with the one-dimensional tube model of the heat transfer fluid to obtain quantitative results regarding the hydrodynamic performance of the heat transfer fluid. This results in a cavity wall temperature distribution as the fluid passes through the receiver tubes that will be influenced by the regimes of flow and heat transfer that evolve (Lin et al., 2018; Zapata et al., 2013). Afterwards, knowledge of the cavity geometry can be used to calculate detailed surface-to-

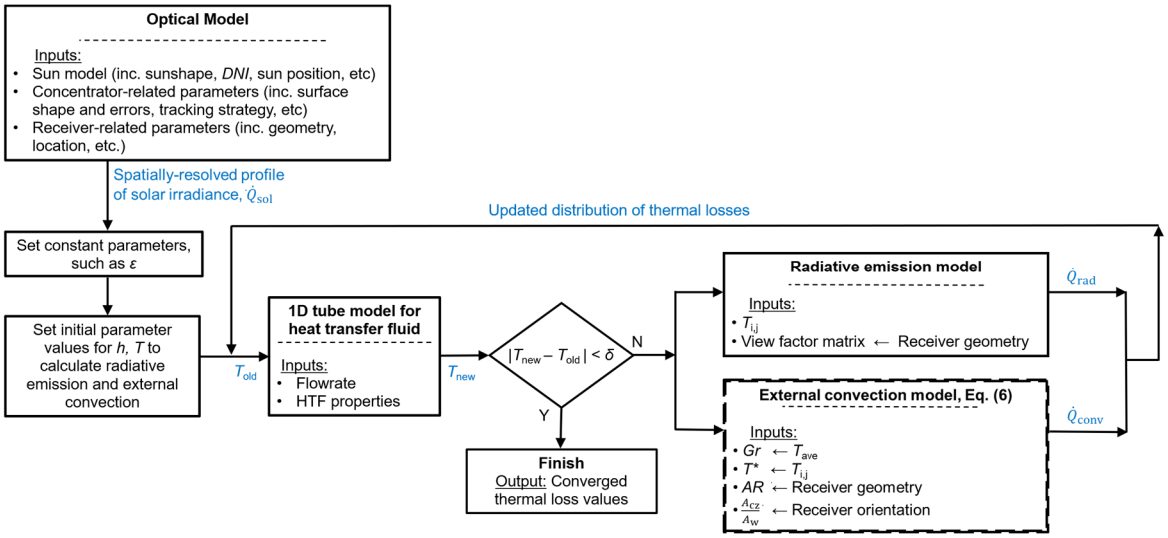

Fig. 15. Flowchart of the iterative energy analysis process to obtain a converged temperature distribution in a solar receiver. The process block relating to the external convection model (shown with the dashed outline) represents the stage at which the proposed correlation of this work, Eq. (6), can be used.

surface view factors which, in conjunction with wall temperature distribution, enables the calculation of radiative emission losses. The dashed process block in Fig. 15 represents the stage at which the correlation proposed in the present work can be used. Input parameters to this correlation include the Grashof number and the temperature non-uniformity factor T^*, both of which can be obtained using the temperature distribution obtained in the previous step of this process. Knowledge of the cavity geometry and orientation allows for the calculation of the aspect ratio, as well as A_{cz}/A_w. The updated values for radiative emission and external convection serve as inputs to the heat transfer fluid model and a new refined temperature distribution on the cavity surface is obtained. This process can be iteratively undertaken until the satisfactory convergence criterion is met.

The usefulness of the proposed correlation is that it can enable the prediction of total convection heat loss from the cavity and an average heat transfer coefficient without the large expenditure of computational resources that are usually needed for numerical solutions relating to heat transfer and flow dynamics within the cavity receiver.

Based on the observations of the present work relating to non-uniform cavity wall temperatures, a possible refinement to the process described above relates to the way in which the average convection heat transfer coefficient is used. In a realistic scenario, this coefficient does not have a uniform value throughout the cavity and it can be argued that it mainly applies to the convective zone surface area A_{cz}. A more accurate use of this coefficient would be to only apply it to this latter area, thereby ensuring that non-uniform temperature distributions would arise based on the input of the convection model in the iterative process. Mere use of the convection heat transfer coefficient for the whole cavity surface area would inhibit this. This subtle point merits further future investigation.

In Section 4.4, the proposed correlation is used to estimate convection heat loss from two example cases of solar cavity receivers, and the values are compared with the relevant experimentally-measured losses. Additionally, to ensure confidence in its use, the convection loss estimate obtained from the proposed correlation of this work is compared to results from other relevant correlations in the literature.

4.4. Application of proposed correlation to large-scale cavity receivers

4.4.1. Cylindrical cavity

The proposed correlation in Section 4.2 is used to estimate natural convection heat loss from a heated cylindrical cavity with length L equal to 0.45 m, cavity diameter D_{cav} equal to 0.3 m and aperture diameter D_{ap} of 0.15m, as reported in Lee et al. (2019). Experimental values of natural convection loss are reported for two different temperature distributions, firstly a uniform temperature distribution and, secondly, the "Rear hotter" case where the section of the cavity closer to the back wall is at a higher temperature than the front section. In both cases, the average cavity temperature is 300°C. The latter case is similar to the temperature distributions encountered in the current work. The Grashof number for the experimental data by Lee et al. (2019) is 7.34×10^7, which is within the range applicable to the proposed correlation of the current work. Table 2 presents the comparison between experimentally-measured convection loss results with estimates obtained from different correlations, including the correlation proposed in this work. Given that the cavity under consideration by Lee et al. (2019) consists of a reduced-diameter aperture, the

Table 2. Comparison of experimental results for a heated cylindrical cavity with estimates from correlations in the literature and the proposed correlation of this work, Eq. (6)

Source of result	Temperature conditions	$\dot{Q}_{conv}$ [W]	Difference
Experimentally measured[a] (Lee et al., 2019)		**431**	**-**
Proposed correlation, Eq. (6) (present work)	Uniform T_w = 300°C	437[c]	1%
Mod. Clausing correlation (Leibfried and Ortjohann, 1995)		454	+5%
Clausing correlation (Clausing et al., 1987)		465	+8%
Experimentally measured[b] (Lee et al., 2019)	Non-uniform T_{max} = 400°C T_{min}= 200°C	**482**	**-**
Proposed correlation, Eq. (6) (present work)		474 [c]	-2%

[a] **Experiment conditions:** Isothermal temperature distribution T^* = 1, θ = 15°, A_{cz} = 0.278 m², A_w = 0.548 m²

[b] **Experiment conditions:** "Rear hotter" temperature distribution T^* = 2.11, Same geometry and inclination as above.

[c] **Note:** Given the reduced aperture of the cavity, the aspect ratio is divided by the ratio of aperture to cavity diameter to better model the influence of the aperture on the flow inside the cavity.

modified Clausing correlation (Leibfried and Ortjohann, 1995) has also been used to estimate the convection heat loss. This is because the latter correlation incorporates length definitions that consider the influence of the aperture lip on the flow patterns in the cavity, thus providing improved estimates of the convection heat loss in comparison to the Clausing correlation. In using the proposed correlation, the aspect ratio is divided by the ratio of aperture to cavity diameter to better model the reduced aperture effect.

As seen in Table 2, in the case of a uniform temperature distribution, the proposed correlation provides an accurate estimate of the convection losses, to within 1% of the reported value. The modified Clausing correlation provides a better estimate of the losses compared with the Clausing correlation, mainly due to its improved characteristic length definition. The estimate provided by the Clausing correlation has a larger error of 8%.

In the case of a non-uniform temperature distribution, the two correlations in the literature discussed here provide the same estimates as those for the uniform temperature distribution case. This is due to the fact that the average temperature, which is based on the maximum and minimum temperature, is equal to that of the uniform temperature distribution case. In contrast, the proposed correlation in this work is able to satisfactorily account for the temperature non-uniformity in the cavity and provide an estimate which is close to the actual reported value, to within ~2%.

4.4.2. Cubical cavity

To further gauge the usefulness of the proposed correlation for different geometries, it is used to estimate convection loss from the 2.18-m cubical cavity studied experimentally by Kraabel (1983). At the reported operating temperature of 750°C, the Grashof number of the convective flow in the cavity is equal to 10^{11}, signifying turbulent natural convection. Table 3 compares the estimates of the convection loss from different correlations with the experimentally-derived result. Based on experimental data reported by Kraabel (1983), the minimum and maximum cavity temperatures are 109°C and 815°C, respectively, resulting in $T^* = 8.8$, when $T_\infty = 18$°C. Given the fully-open aperture of this geometry, the height of the cubical cavity, rather than the literal definition of diameter, is taken to be the dimension of interest when calculating the characteristic length. As such, for the horizonal-facing cubical cavity of interest, $L_c = \frac{3}{2}L$. The value of convection loss obtained by using Eq. (6) is 227 kW, equating to an error of ~3% in estimating the experimentally measured value of 220 kW for the cubical cavity.

The correlation proposed by Clausing et al. (1987) has been reported by Yuan et al. (2015) to give an estimate of 109 kW as the convection losses for the cavity. This value underestimates the losses by 50%. By implementing the resources developed as part of the present work, we found that the Clausing correlation provides a convection heat loss estimate of 195 kW, which is within 11% of the experimental results and could be assumed to fall within the experimental error of the original study. Given that a cubical cavity, albeit with a dimension of L = 0.4 m, was used by Clausing to develop the database for the respective correlation, the estimate of losses with a smaller error could have been anticipated from the use of this correlation. Furthermore, the modified Clausing correlation (Leibfried and Ortjohann, 1995), which uses a similar formulation to the Clausing correlation, could provide insight into the estimates for the cubical cavity. Table 3 shows that the modified Clausing correlation provides an estimate of 196 kW for the convection losses. The comparison presented here highlights the difficulties and inaccuracies that can arise in the correct calculation of the parameters used in the Clausing correlation, particularly those associated with the inclusion of the iteratively-solved implicit function b (refer to Nomenclature section for the full formulation of this function) related to the modelling of bulk air temperature inside the

Table 3. Comparison of experimental results for a heated cubical cavity with estimates from correlations previously reported in the literature and the proposed correlation of this work, Eq. (6).

Source of result	$\dot{Q}_{conv}$ [kW]	Difference
Experimentally measured (Kraabel, 1983)	**220**	**-**
Proposed correlation, Eq. (6) (present work)	227	+ 3%
Clausing et al. (1987) correlation estimate, as reported by Yuan et al. (2015)	109	-50%
Clausing et al. (1987) correlation estimate, as calculated in this study	195	-11%
Modified Clausing correlation (Leibfried and Ortjohann, 1995)	196	-11%

cavity. For this reason, the complexity of the Clausing correlation could be deemed as one of its drawbacks. The proposed correlation of this work is envisaged to be an accurate and easy-to-use alternative to the Clausing correlation.

Given that the Grashof number of the flow in the cavity falls outside the applicable range for the proposed correlation of this work, namely $Gr = 8.41\times10^7$, the remarkably good estimate that it provides is pleasing. It would seem that the T^* and A_{cz}/A_w factors in the correlation are instrumental in modelling the important parameters influencing convection heat loss in the cavity. Furthermore, despite the fact that the correlation proposed has been developed from experimental datasets using cylindrical cavities, it has the potential to predict convective heat losses from other geometries and scales. For this reason, examining detailed data from other cavities can help in further refining the parameters of the proposed correlation and in this way, improve the scope of its applicability.

Conclusions

This paper aimed to incorporate temperature non-uniformity into predictions of convection heat loss from solar cavity receivers. To meet this aim, a model cylindrical cavity receiver was studied experimentally at operating temperatures up to 650°C with differing degrees of wall temperature non-uniformity. Thermal losses were calculated using a combined analytical and experimental approach. The following conclusions can be enumerated:

1. The novel method that was used to introduce large temperature inhomogeneity along the cavity walls consisted of varying the arrangement of and power input to heating coils on the outer surface of cavities with different aspect ratio. These temperature profiles could be considered to be more representative of conditions observed in realistic solar thermal cavity receivers, in comparison to temperature profiles studied in previous investigations of convection loss.
2. Significantly-reduced radiative losses were observed in the case of a cavity with the largest temperature inhomogeneity. For the same aspect ratio, a cavity with a more non-uniform temperature distribution was observed to have a smaller fraction of the total power input lost due to convection. For the non-isothermal cavities studied in this work, increasing the aspect ratio from one to two resulted in reduced convection loss at all inclinations other than horizontal. This trend cannot be observed if isothermal boundary conditions are imposed.
3. Comparison of the non-isothermal experimental results of this work with estimates obtained from the use of correlations from the literature showed that the Clausing correlation provided a reasonable prediction of convection heat loss, despite its complexity of use. However, other widely–used correlations with less complexity than that of Clausing presented differing degrees of discrepancy and, in some cases, exhibited incorrect trends.
4. A new Nusselt number correlation was proposed that takes into account the non-uniformity of the temperature distribution in the cavity through the use of a dimensionless temperature factor T^*. As observed during the analysis of experimental results, the fraction of the total cavity surface area taken up by the convective zone at each inclination angle was found to be important in predicting the losses, leading to the inclusion of this parameter in the correlation.

5. The correlation predicts 92% of the experimental data produced in this and three other experimental studies in the literature to within ±30%, and has been found to predict results with equal, if not better, accuracy than the Clausing correlation which has become the gold-standard for convection loss correlations. The success of the proposed correlation suggests that temperature inhomogeneity has a significant effect on convective heat losses.

6. Although the correlation proposed in this work has been developed from experimental datasets using cylindrical cavities, it was shown to have the potential to predict convective heat losses from other geometries and scales, such as a 2.18-m cubical cavity. Further work examining data from other geometries would prove helpful in refining the proposed correlation parameters, thus allowing for better estimates of convection heat loss in solar cavity receivers.

7. The proposed correlation has been defined in a significantly more usable form than the Clausing correlation, and can be easily used in integrated analysis of cavity receiver heat loss.

Acknowledgements

This work was funded by the Australian Renewable Energy Agency (ARENA) for the project Improved High-Temperature Receivers for Dish Concentrators (1-UFA006). EAS is thankful to the Australian government for an Australian Postgraduate Award Scholarship. GH was supported by Australian Research Council Fellowship FT100100869. Provision of access to the Australian National University's Geophysical Fluid Dynamics Laboratory and technical workshop assistance at the Research School of Earth Sciences is gratefully acknowledged. We thank the anonymous reviewers for their feedback, which has improved the clarity and quality of our work.

Nomenclature

A surface area, m^2

AR aspect ratio (= cavity length/diameter), -

b implicit function in Clausing et al. (1987)

$$= 1 - 1.57\left[\frac{g(Ra)\cdot f(Ra,T_w/T_\infty)\cdot b\cdot\left(k_f/k_\infty\right)}{\left(Ra_\infty\cdot Pr_\infty\cdot L_{ap}\Big/\left(L_{ap}\cdot\cos\theta+L_{ap}/2\right)\right)^{\frac{1}{2}}\cdot\left(A_{ap}/A_{cz}\right)}\right]^{\frac{2}{3}}$$

D diameter, m

$E_{b,i}$ blackbody emissive power of surface i, W/m^2

F_{ij} fraction of radiant energy leaving surface i and reaching surface j, -

g gravitational acceleration constant, m/s^2

J_i radiosity of surface i , W/m^2

k thermal conductivity, W/m·K

L length, m

P total power input, W

$\dot{Q}$ heat transfer rate, W

T temperature, °C

T^* dimensionless temperature, $= (T_{max} - T_\infty)/(T_{min} - T_\infty)$

x axial distance along cavity wall, m

Gr Grashof number, -

Nu Nusselt number, -

Ra Rayleigh number, -

R_a Arithmetic mean surface roughness, μm

Greek symbols

$ß$ coefficient of volumetric expansion, 1/K

ε thermal emissivity, -

δ uncertainty, -

θ inclination angle, degree

υ kinematic viscosity, m^2/s

Subscripts

∞ ambient condition

ap aperture

ave average

b bulk cavity air properties

c characteristic parameter

cav cavity-based parameter

cond conduction

conv convection

cz convective zone (i.e. aperture area + area of lateral and back wall surface of cavity below free-shear plane)

f thermophysical property based on film temperature

ins insulation

min minimum value

max maximum value

rad radiation

sol solar

w wall area-based parameter

$\perp$ vertical component of a geometric length

References

Abbasi-Shavazi, E., Hughes, G.O., Pye, J.D., 2015. Investigation of heat loss from a solar cavity receiver. Energy Procedia 69, 269-278.

Apley, W.J., 1978, Systems Analysis of Solar Thermal Power Systems. Report on Task 1 - Determination and Characterization of Solar Thermal Conversion Options. Report No. PNL-2693, Battelle Pacific Northwest Laboratory, Richland, Washington.

Asselineau, C.-A., 2018. Geometrical Optimisation of Receivers for Concentrating Solar Thermal Systems. PhD thesis, College of Engineering and Computer Science, The Australian National University, Canberra, Australia.

Asselineau, C.-A., Zapata, J., Pye, J., 2015. Integration of Monte-Carlo ray tracing with a stochastic optimisation method: application to the design of solar receiver geometry. Optics express 23(11), A437-A443.

ASTRI, 2017, ASTRI Milestone 12 Report - For Public Dissemination. Australian Renewable Energy Agency, Canberra, Australia.

Behar, O., Khellaf, A., Mohammedi, K., 2013. A review of studies on central receiver solar thermal power plants. Renewable and Sustainable Energy Reviews 23, 12–39.

Boehm, R.F., 1987. A review of convective loss data from solar central receivers. Journal of Solar Energy Engineering 109, 101–107.

Braun, G.W., Edelstein, R.B., 1980. Review of the U.S. department of energy's solar thermal program. Revue de Physique Appliquée 15(7), 1219–1228.

Cagnoli, M., de la Calle, A., Pye, J., Savoldi, L., Zanino, R., 2019. A CFD-supported dynamic system-level model of a sodium-cooled billboard-type receiver for central tower CSP applications. Solar Energy 177, 576-594.

Cagnoli, M., Savoldi, L., Zanino, R., Zaversky, F., 2017. Coupled optical and CFD parametric analysis of an open volumetric air receiver of honeycomb type for central tower CSP plants. Solar Energy 155, 523-536.

Chakroun, W., 2004. Effect of boundary wall conditions on heat transfer for fully opened tilted cavity. Journal of Heat Transfer 126, 915-923.

Chakroun, W., Elsayed, M., Al-Fahed, S., 1997. Experimental measurements of heat transfer coefficient in a partially/fully opened tilted cavity.

Chakroun, W., Quadri, M.M.A., 2002. Heat transfer measurements for smooth and rough tilted semi-cylindrical cavities. International journal of thermal sciences 41(2), 163-172.

Chen, K.S., Humphrey, J.A.C., Sherman, F.S., 1985. Free and mixed convective flow of air in a heated cavity of variable rectangular cross section and orientation. Philosophical Transactions of the Royal Society of London. Series A, Mathematical and Physical Sciences 316(1535), 57–84.

Clausing, A., Kempka, S., 1981. The influences of property variations on natural convection from vertical surfaces. Journal of Heat Transfer 103(4), 609-612.

Clausing, A.M., 1981. An analysis of convective losses from cavity solar central receivers. Solar Energy 27(4), 295–300.

Clausing, A.M., 1982. Advantages of a cryogenic environment for experimental investigations of convective heat transfer. International Journal of Heat and Mass Transfer 25(8), 1255-1257.

Clausing, A.M., 1983. Convective losses from cavity solar receivers - Comparisons between analytical predictions and experimental results. Journal of Solar Energy Engineering 105, 29–33.

Clausing, A.M., Waldvogel, J.M., Lister, L.D., 1987. Natural Convection From Isothermal Cubical Cavities With a Variety of Side-Facing Apertures. Journal of Heat Transfer 109, 407–412.

Dalziel, S.B., Hughes, G.O., Sutherland, B.R., 2000. Whole-field density measurements by 'synthetic schlieren'. Experiments in Fluids 28(4), 322–335.

Falcone, P., 1981, Convective losses from solar central receivers: proceedings of a DOE/SERI/SNLL workshop. SAND-81-8014, Sandia National Laboratories, Livermore, California.

Falcone, P.K., 1986, A handbook for solar central receiver design. Report No. SAND-86-8009, Sandia National Laboratories, Livermore, California.

Fang, J., Tu, N., Torres, J.F., Wei, J., Pye, J.D., 2019. Numerical investigation of the natural convective heat loss of a solar central cavity receiver with air curtain. Applied Thermal Engineering 152, 147–159.

Faw, R., Dullforce, T., 1982. Holographic interferometry measurement of convective heat transport beneath a heated horizontal circular plate in air. International Journal of Heat and Mass Transfer 25(8), 1157-1166.

Flesch, R., Grobbel, J., Stadler, H., Uhlig, R., Hoffschmidt, B., 2015. Reducing the convective losses of cavity receivers, SolarPACES 2015. AIP Publishing, Cape Town, South Africa.

Flesch, R., Stadler, H., Uhlig, R., Hoffschmidt, B., 2015. On the influence of wind on cavity receivers for solar power towers: An experimental analysis. Applied Thermal Engineering 87, 724-735.

Harris, J.A., Lenz, T.G., 1985. Thermal performance of solar concentrator/cavity receiver systems. Solar Energy 34(2), 135–142.
Ho, C.K., Mahoney, A.R., Ambrosini, A., Bencomo, M., Hall, A., Lambert, T.N., 2012. Characterization of Pyromark 2500 for high temperature solar receivers, ASME 2012 6th International Conference on Energy Sustainability Collocated with the ASME 2012 10th International Conference on Fuel Cell Science, Engineering and Technology Conference (ESFuelCell2012). American Society of Mechanical Engineers, San Diego, California, pp. 509–518.
Holman, J.P., 2010. Heat Transfer, 10th ed. McGraw-Hill Inc., Boston.
Howell, J.R., Siegel, R., Menguc, M.P., 2010. Thermal Radiation Heat Transfer, 5th ed. Taylor and Francis/CRC, New York.
Hughes, G., Pye, J., Kaufer, M., Abbasi-Shavazi, E., Zhang, J., McIntosh, A., Lindley, T., 2016. Reduction of convective losses in solar cavity receivers, AIP Conference Proceedings. AIP Publishing, p. 030023.
IEA, 2018. World Energy Balances: Overview. https://webstore.iea.org/world-energy-balances-2018-overview. (Accessed 20-03-2019).
Jilte, R.D., Kedare, S.B., Nayak, J.K., 2013. Natural convection and radiation heat loss from open cavities of different shapes and sizes used with dish concentrator. Mechanical Engineering Research 3(1), 25–43.
Jilte, R.D., Nayak, J.K., Kedare, S.B., 2017. Experimental investigation on heat losses from differentially heated cylindrical cavity receiver used in paraboloid concentrator. Journal of Solar Energy Engineering 139(3), 0310131–03101313.
Koenig, A.A., Marvin, M., 1981, Convection Heat Loss Sensitivity in Open Cavity Solar Receivers: Final Report. DOE Contract No. EG77-C-04-3985, Department of Energy, Oak Ridge, Tennessee.
Kolb, G.J., 2011, An Evaluation of Possible Next-Generation High-Temperature Molten-Salt Power Towers. Report No. SAND2011-9320, Sandia National Laboratories, Albuquerque, New Mexico.
Kraabel, J.S., 1983. An Experimental Investigation of the Natural Convection From a Side-Facing Cubical Cavity, Proceedings of the ASME JSME Thermal Engineering Joint Conference. Honolulu, Hawaii, pp. 299–306.
Kribus, A., Doron, P., Rubin, R., Karni, J., Reuven, R., Duchan, S., Taragan, E., 1999. A multi-stage solar receiver: The route to high temperature. Solar Energy 67(1–3), 3–11.
Lee, K.L., Chinnici, A., Jafarian, M., Arjomandi, M., Dally, B., Nathan, G., 2018. Experimental investigation of the effects of wind speed and yaw angle on heat losses from a heated cavity. Solar Energy 165, 178–188.
Lee, K.L., Chinnici, A., Jafarian, M., Arjomandi, M., Dally, B., Nathan, G., 2019. The influence of wall temperature distribution on the mixed convective losses from a heated cavity. Applied Thermal Engineering 155, 157–165.
Lee, K.L., Jafarian, M., Ghanadi, F., Arjomandi, M., Nathan, G.J., 2017. An investigation into the effect of aspect ratio on the heat loss from a solar cavity receiver. Solar Energy 149, 20–31.
Leibfried, U., Ortjohann, J., 1995. Convective Heat Loss from Upward and Downward-Facing Cavity Solar Receivers: Measurements and Calculations. Journal of Solar Energy Engineering 117(2), 75–84.
Lin, M., Reinhold, J., Monnerie, N., Haussener, S., 2018. Modeling and design guidelines for direct steam generation solar receivers. Applied Energy 216, 761–776.
Liovic, P., Kim, J.-S., Hart, G., Stein, W., 2014. Wind dependence of energy losses from a solar gas reformer. Applied Thermal Engineering 63(1), 333-346.
Ma, R.Y., 1993, Wind effects on convective heat loss from a cavity receiver for a parabolic concentrating solar collector. Report No. SAND-92-7293, Sandia National Laboratories, Albuquerque, New Mexico.
Maag, G., Falter, C., Steinfeld, A., 2011. Temperature of a quartz/sapphire window in a solar cavity-receiver. Journal of Solar Energy Engineering 133(1), 014501.
McDonald, C.G., 1995, Heat loss from an open cavity. Report Number SAND95-2939, Sandia National Laboratories, Albuquerque, New Mexico.
Mehos, M., Turchi, C., Jorgenson, J., Denholm, P., Ho, C.K., Armijo, K., 2016, On the Path to SunShot: Advancing Concentrating Solar Power Technology, Performance, and Dispatchability. Report No. NREL/TP-5500-65688 SAND-2016-2237 EERE Publication and Product Library, Golden, Colorado.
Montiel-Gonzalez, M., Hinojosa, J., Villafan-Vidales, H., Bautista-Orozco, A., Estrada, C., 2015. Theoretical and experimental study of natural convection with surface thermal radiation in a side open cavity. Applied Thermal Engineering 75, 1176-1186.
Najafabadi, H.A., Ozalp, N., 2018. An advanced modeling and experimental study to improve temperature uniformity of a solar receiver. Energy 165 (Part B), 984–998.
Najafabadi, H.A., Ozalp, N., Ophoff, C., Moens, D., 2019. An experimental study on temperature control of a solar receiver under transient solar load. Solar Energy 186, 52-59.
Ngo, L., Bello-Ochende, T., Meyer, J.P., 2015. Numerical modelling and optimisation of natural convection heat loss suppression in a solar cavity receiver with plate fins. Renewable Energy 74, 95–105.

Ortega, J.D., Christian, J.M., Ho, C.K., 2017. Design and Testing of a Novel Bladed Receiver, ASME 2017 11th International Conference on Energy Sustainability collocated with the ASME 2017 Power Conference Joint With ICOPE-17, the ASME 2017 15th International Conference on Fuel Cell Science, Engineering and Technology, and the ASME 2017 Nuclear Forum. American Society of Mechanical Engineers, p. V001T005A007.

Paitoonsurikarn, S., Lovegrove, K., Hughes, G., Pye, J., 2011. Numerical investigation of natural convection loss from cavity recievers in solar dish applications. Journal of Solar Energy Engineering 133, 0210041.

Polat, O., Bilgen, E., 2003. Conjugate heat transfer in inclined open shallow cavities. International Journal of Heat and Mass Transfer 46(9), 1563-1573.

Prakash, M., 2014. Numerical study of natural convection heat loss from cylindrical solar cavity receivers. ISRN Renewable Energy 2014.

Prakash, M., Kedare, S.B., Nayak, J.K., 2009. Investigations on heat losses from a solar cavity receiver. Solar Energy 83, 157–170.

Prakash, M., Kedare, S.B., Nayak, J.K., 2010. Determination of stagnation and convective zones in a solar cavity receiver. International Journal of Thermal Sciences 49, 680–691.

Pye, J., Abbasi, E., Arjomandi, M., Coventry, J., Ghanadi, F., Hughes, G., Kilm, J., Ma, L., Shirazi, A., Torres, J.F., 2018. Towards Testing of a Second-Generation Bladed Receiver, Proceedings of the 2018 SolarPACES International Conference. Casablanca, Morocco.

Pye, J., Coventry, J., Venn, F., Zapata, J., Abbasi, E., Asselineau, C.A., Burgess, G., Hughes, G., Logie, W.R., 2016. Experimental testing of a high-flux cavity receiver, AIP Conference Proceedings. AIP Publishing, p. 110011.

Pye, J., Hughes, G., Abbasi, E., Asselineau, C.A., Burgess, G., Coventry, J., Logie, W., Venn, F., Zapata, J., 2015. Development of a higher-efficiency tubular cavity receiver for direct steam generation on a dish concentrator, SolarPACES. AIP Publishing, Cape Town.

Radziemska, E., Lewandowski, W., 2001. Heat transfer by natural convection from an isothermal downward-facing round plate in unlimited space. Applied Energy 68(4), 347-366.

Ries, H., Kribus, A., Karni, J., 1995. Non-isothermal Receivers. Journal of Solar Energy Engineering 117, 259–261.

Samanes, J., García-Barberena, J., Zaversky, F., 2015. Modeling solar cavity receivers: a review and comparison of natural convection heat loss correlations. Energy Procedia 69, 543–552.

Shen, Z.-G., Wu, S.-Y., Xiao, L., Li, D.-L., Wang, K., 2015. Experimental and numerical investigations of combined free convection and radiation heat transfer in an upward-facing cylindrical cavity. International Journal of Thermal Sciences 89, 314-326.

Shuai, Y., Xia, X.-L., Tan, H.-P., 2008. Radiation performance of dish solar concentrator/cavity receiver systems. Solar Energy 82(1), 13–21.

Siebers, D., Moffatt, R., Schwind, R., 1985. Experimental, variable properties natural convection from a large, vertical, flat surface. Journal of Heat Transfer 107(1), 124-132.

Siebers, D.L., Kraabel, J.S., 1984, Estimating conective energy losses from solar central receivers. Sandia National Laboratories, Albuquerque.

Steinfeld, A., Epstein, M., González-Aguilar, J., 2017. Progress in Solar Energy special issue: Advances in solar thermochemistry. Solar Energy 156, 1-2.

Stine, W.B., McDonald, C.G., 1989. Cavity receiver convective heat loss, International Solar Energy Society Solar World Congress. Kobe, Japan, pp. 1318–1322.

Taumoefolau, T., 2004. Experimental investigation of convection loss from a model solar concentrator cavity receiver. M. Phil thesis, Department of Engineering & Computer Science, The Australian National University, Canberra, Australia.

Taumoefolau, T., Paitoonsurikarn, S., Hughes, G., Lovegrove, K., 2004. Experimental investigation of natural convection heat loss from a model solar concentrator cavity receiver. Journal of Solar Energy Engineering 126, 801–807.

Torres, J.F., Ghanadi, F., Nock, I., Arjomandi, M., Pye, J., 2018. Mixed convection around a tilted cuboid with an isothermal sidewall at moderate Reynolds numbers. International Journal of Heat and Mass Transfer 119, 418–432.

Torres, J.F., Ghanadi, F., Wang, Y., Arjomandi, M., Pye, J., 2020. Mixed convection and radiation from an isothermal bladed structure,. International Journal of Heat and Mass Transfer 147.

Tu, N., Wei, J., Fang, J., 2013. Experimental and numerical study on the thermal performance of a water/steam cavity receiver. Energies 6, 1198-1216.

Uhlig, R., Flesch, R., Gobereit, B., Giuliano, S., Liedke, P., 2014. Strategies enhancing efficiency of cavity receivers. Energy Procedia 49, 538-550.

Van den Langenbergh, L., Ophoff, C., Ozalp, N., 2015. An iris mechanism driven temperature control of solar thermal reactors, First Thermal and Fluid Engineering Summer Conference (TFESC). Begel House Inc., New York, USA, pp. 9-12.
Wang, Y., Coventry, J., Pye, J., 2019. Optical and radiation considerations in bladed receiver designs for central tower systems, AIP Conference Proceedings. AIP Publishing, p. 030063.
Wang, Y., Potter, D., Asselineau, C.-A., Corsi, C., Wagner, M., Blanco, M., Kim, J.-S., Pye, J., 2018. Comparison of optical modelling tools for sunshape and surface slope error, AIP Conference Proceedings. AIP Publishing, p. 210020.
Wu, S.-Y., Guan, J.-Y., Xiao, L., Shen, Z.-G., Xu, L.-H., 2013. Experimental investigation on heat loss of a fully open cylindrical cavity with different boundary conditions. Experimental Thermal and Fluid Science 45, 92–101.
Wu, S.-Y., Guo, F.H., Xiao, L., 2014. Numerical investigation on combined natural convection and radiation heat losses in one side open cylindrical cavity with constant heat flux. International Journal of Heat and Mass Transfer 71, 573-584.
Wu, S.-Y., Shen, Z.-G., Xiao, L., 2015a. Experimental investigation and uncertainty analysis on combined heat losses characteristics of a cylindrical cavity with only bottom wall heated at constant heat flux. Heat Transfer Engineering 36(6), 539-552.
Wu, S.-Y., Shen, Z.-G., Xiao, L., Li, D.-L., 2015b. Experimental study on combined convective heat loss of a fully open cylindrical cavity under wind conditions. International Journal of Heat and Mass Transfer 83, 509-521.
Wu, S.-Y., Xiao, L., Cao, Y., Li, Y.-R., 2010. Convection heat loss from cavity receiver in parabolic dish solar thermal power system - A review. Solar Energy 84, 1342-1355.
Wu, W., Amsbeck, L., Buck, R., Waibel, N., Langner, P., Pitz-Paal, R., 2014. On the influence of rotation on thermal convection in a rotating cavity for solar receiver applications. Applied Thermal Engineering 70, 694–704.
Xamán, J., Álvarez, G., Hinojosa, J., Flores, J., 2009. Conjugate turbulent heat transfer in a square cavity with a solar control coating deposited to a vertical semitransparent wall. International Journal of Heat and Fluid Flow 30(2), 237-248.
Xiao, L., Guo, F.-W., Wu, S.-Y., Chen, Z.-L., 2020. A comprehensive simulation on optical and thermal performance of a cylindrical cavity receiver in a parabolic dish collector system. Renewable Energy 145, 878-892.
Xiao, L., Wu, S.-Y., Li, Y.-R., 2012. Numerical study on combined free-forced convection heat loss of solar cavity receiver under wind environments. International Journal of Thermal Sciences 60, 182–194.
Yeh, K.C., Hughes, G., Lovegrove, K., 2005. Modelling the convective flow in solar thermal receivers, 43rd Conference of the Australia and New Zealand Solar Energy Society (ANZSES). Dunedin, New Zealand.
Yuan, J.K., Ho, C.K., Christian, J.M., 2015. Numerical simulation of natural convection in solar cavity receivers. Journal of Solar Energy Engineering 137(3), 031004.
Zapata, J.I., Pye, J., Lovegrove, K., 2013. A transient model for the heat exchange in a solar thermal once through cavity receiver. Solar Energy 93, 280-293.
Zhang, H.L., Baeyens, J., Degrève, J., Cacèresc, G., 2013. Concentrated solar power plants: Review and design methodology. Renewable and Sustainable Energy Reviews 22, 466–481.
Zhang, J.J., Pye, J.D., Hughes, G.O., 2015. Active air flow control to reduce cavity receiver heat loss, ASME 2015 9th International Conference on Energy Sustainability collocated with the ASME 2015 Power Conference, the ASME 2015 13th International Conference on Fuel Cell Science, Engineering and Technology, and the ASME 2015 Nuclear Forum. American Society of Mechanical Engineers, p. V001T005A023.

Appendix A

Table A1. Subset of dataset relating to near-constant total flux experiments P=156 W (±5%).

Note: 1) Data from this table is used in the development and interpretation of Fig. 9

2) The temperatures reported for the convective and stagnation zones and the whole cavity relate to surface temperatures rather than air temperature.

									Convective zone			Stagnation zone			Whole cavity			
θ [deg]	AR [-]	P_{heat} [W]	$\dot{Q}_{rad}$ [W]	$\dot{Q}_{cond}$ [W]	$\dot{Q}_{conv}$ [W]	$\dot{Q}_{passive\ zone}$ [W]	A_{cz} [m²]	A_{cz}/A_w [-]	T_{ave} [°C]	T_{max} [°C]	T_{min} [°C]	T_{ave} [°C]	T_{max} [°C]	T_{min} [°C]	T_{ave} [°C]	$T_{ave\ (heated)}$ [°C]	T_{max} [°C]	T_{min} [°C]
	2	150	76.5	52.5	21.0	-	0.0054	0.11	418.1	418.1	418.1	465.5	500.1	413.8	465.8	-	500.1	413.8
90	1	160	86.2	38.6	35.3	-	0.0054	0.20	455.0	455.5	454.5	487.0	498.8	454.5	477.4	-	498.8	454.5
	2*	164	24.9	40.5	19.9	78.7	0.0054	0.11	203.0	203.7	201.5	341.8	497.8	201.5	353.6	474.0	497.8	201.5
	2	150	64.6	47.1	38.3	-	0.0117	0.24	367.2	367.2	367.2	449.1	481.8	377.2	441.9	-	481.8	367.2
60	1	160	73.3	33.6	53.2	-	0.0117	0.43	411.5	418.2	404.9	461.1	480.0	436.3	451.2	-	480.0	404.9
	2*	164	22.6	39.3	33.5	68.7	0.0117	0.24	183.8	198.9	168.4	352.6	492.2	199.8	342.4	467.2	492.2	168.4
	2	150	48.8	37.4	63.8	-	0.0242	0.50	366.2	425.4	321.6	414.4	439.6	361.4	396.4	-	439.6	321.6
30	1	160	56.5	25.2	78.4	-	0.0217	0.80	397.1	422.7	366.0	415.3	441.3	386.7	406.2	-	441.3	366.0
	2*	164	19.5	34.8	51.8	57.8	0.0242	0.50	225.4	460.1	149.6	363.3	473.2	198.4	322.3	443.7	473.2	149.6
	2	150	31.1	21.2	97.6	-	0.0541	1.11	315.9	355.5	275.5	-	-	-	315.9	-	355.5	275.5
0	1	160	48.0	19.8	92.2	-	0.0325	1.20	378.5	412.8	345.2	-	-	-	378.5	-	412.8	345.2
	2*	164	12.8	21.0	95.7	34.4	0.0541	1.11	244.3	407.5	122.7	-	-	-	267.9	370.5	407.5	122.7

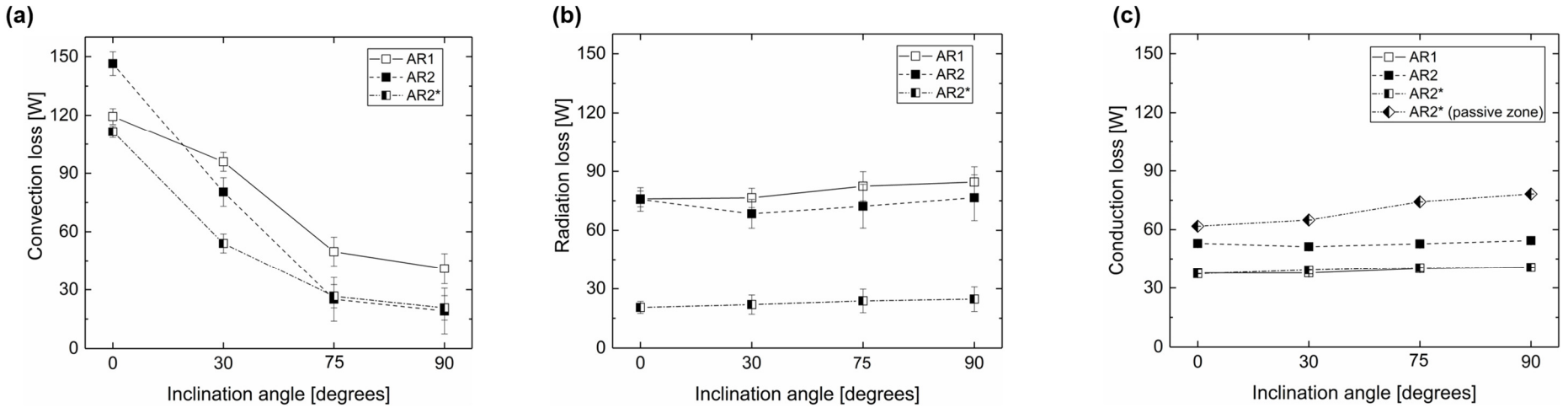

Fig. A1. Breakdown of thermal losses, including error bars, for experiments with near-constant peak temperature ~500°C. (a) Convection loss (b) Radiation loss, (c) Conduction loss, including passive zone heat loss.

Table A2. Subset of datasets relating to constant peak temperature experiments (~500°C).
Notes: 1) Data from this table is used in the development and interpretation of Fig. A1
2) The temperatures reported for the convective and stagnation zones and the whole cavity relate to surface temperatures rather than air temperature.

									Convection zone			Stagnation zone			Whole cavity			
θ [deg]	AR [-]	P_{heat} [W]	$\dot{Q}_{rad}$ [W]	$\dot{Q}_{cond}$ [W]	$\dot{Q}_{conv}$ [W]	$\dot{Q}_{passive\ zone}$ [W]	A_{cz} [m²]	A_{cz}/A_w [-]	T_{ave} [°C]	T_{max} [°C]	T_{min} [°C]	T_{ave} [°C]	T_{max} [°C]	T_{min} [°C]	T_{ave} [°C]	$T_{ave\ (heated)}$ [°C]	T_{max} [°C]	T_{min} [°C]
	2	150	76.5	54.4	19.1	-	0.0054	0.11	418.1	418.1	418.1	465.5	500.1	413.8	465.8	-	500.1	413.8
90	1	166	84.6	40.6	40.9	-	0.0054	0.20	444.9	445.5	444.1	483.4	495.0	451.5	471.8	-	495.0	444.1
	2*	164	24.7	40.5	20.7	78.2	0.0054	0.11	201.2	201.9	199.9	346.8	496.9	204.3	352.3	473.0	496.9	199.9
	2	150	72.2	52.7	25.1	-	0.0083	0.17	395.8	395.8	395.8	457.7	495.1	395.8	458.4	-	495.1	395.8
75	1	172	82.4	39.9	49.7	-	0.0083	0.31	425.6	425.6	425.6	472.9	495.3	434.5	468.2	-	495.3	425.6
	2*	165	23.8	40.4	26.6	74.2	0.0083	0.17	189.6	193.4	181.9	343.9	496.4	202.0	348.7	472.2	496.4	181.9
	2	200	68.4	51.2	80.4	-	0.0242	0.50	421.1	486.4	371.7	471.2	500.4	413.4	452.2	-	500.4	371.7
30	1	210	76.5	37.6	95.9	-	0.0217	0.80	445.8	476.5	407.3	465.3	495.5	434.3	455.5	-	495.5	407.3
	2*	180	21.9	39.2	54.0	64.9	0.0242	0.50	237.7	484.5	158.1	381.4	497.1	208.1	339.0	466.5	497.1	158.1
	2	275	75.7	52.9	146.4	-	0.0541	1.11	459.1	510.6	401.7	-	-	-	459.1	-	510.6	401.7
0	1	233	76.0	37.6	119.4	-	0.0325	1.20	453.8	495.3	416.0	-	-	-	453.8	-	495.3	416.0
	2*	231	20.5	37.2	111.5	61.7	0.0541	1.11	302.4	498.4	155.7	-	-	-	331.2	455.9	498.4	155.7

Appendix B

Figure B1 presents statistics relating to the correlation proposed in this work. Note the following convention, when referring to the Parameters table in Table B1:

$$Nu = c.Gr^{n}\left(\frac{T_{\max}-T_{\infty}}{T_{\min}-T_{\infty}}\right)^{m}_{\text{cavity}}\left(\frac{A_{\text{cz}}}{A_{\text{w,total}}}\right)^{p}\left(\frac{L}{D_{\text{ap}}}\right)^{q} \qquad \text{(Eq. B1)}$$

Table B1. Statistical analysis relating to the correlation developed as part of this work, as described in Section 4.1.

Parameters

		Unit	Value	Fixed	Standard Error	t-Value	Prob>|t|	95% LCL	95% UCL	Dependency	CI Half-Width	Lower Bound	Upper Bound
Nu	c		0.12646	N	0.00125	101.10216	0	0.12398	0.12894	0.55353	0.00248	--	--
	n		0.333	Y	0	--	--	0.333	0.333	0	0	--	--
	m		0.10955	N	0.02319	4.72385	7.27024E-6	0.06356	0.15554	0.49511	0.04599	--	--
	p		0.79473	N	0.02036	39.03993	0	0.75436	0.8351	0.06289	0.04037	--	--
	q		-0.51595	N	0.02323	-22.21153	0	-0.56202	-0.46989	0.54352	0.04606	--	--

Reduced Chi-sqr = 1.41636716276
COD(R^2) = 0.98876193616977
Iterations Performed = 6
Total Iterations in Session = 6
Fit converged - Chi-sqr no longer changed.
Some parameter values were fixed.
Standard Error was scaled with square root of reduced Chi-Sqr.

Statistics

	Nu
Number of Points	108
Degrees of Freedom	104
Reduced Chi-Sqr	1.41637
Residual Sum of Squares	147.30218
R Value	0.99437
R-Square(COD)	0.98876
Adj. R-Square	0.98844
Root-MSE (SD)	1.19011
Number of Iterations	6
Fit Status	Succeeded(101)

Fit Status Code :
101 : Fit converged - Chi-sqr no longer changed.

Summary

	c		n		m		p		q		Statistics	
	Value	Standard Error	Value	Standard Error	Value	Standard Error	Value	Standard Error	Value	Standard Error	Reduced Chi-Sqr	Adj. R-Square
Nu	0.12646	0.00125	0.333	0	0.10955	0.02319	0.79473	0.02036	-0.51595	0.02323	1.41637	0.98844